HURRICANE WIND SPEED AND RAIN RATE RETRIEVAL ALGORITHM FOR THE STEPPED FREQUENCY MICROWAVE RADIOMETER

by

RUBA AKRAM AMARIN
B.S. Princess Sumaya University for Technology, 2004

A thesis submitted in partial fulfillment of the requirements
Degree of Master of Science
in the School of Electrical Engineering and Computer Science
in the College of Engineering and Computer Science
University of Central Florida
Orlando, Florida

Summer Term
2006

ABSTRACT

This thesis presents the development and validation of the Hurricane Imaging Retrieval Algorithm (HIRA) for the measurement of oceanic surface wind speed and rain rate in hurricanes. The HIRA is designed to process airborne microwave brightness temperatures from the NOAA, Stepped Frequency Microwave Radiometer (SFMR), which routinely collects data during NOAA hurricane hunter aircraft flights. SFMR measures wind speeds and rain rates at nadir only, but HIRA will soon be integrated with an improved surface wind speed model for expanded utilization with next generation microwave hurricane imagers, such as the Hurricane Imaging Radiometer (HIRad). HIRad will expand the nadir only measurements of SFMR to allow the measurement of hurricane surface winds and rain over a wide swath

Results for the validation of HIRA retrievals are presented using SFMR brightness temperature data for 22 aircraft flights in 5 hurricanes during 2003-2005. Direct comparisons with the standard NOAA SFMR empirical algorithm provided excellent results for wind speeds up to 70 m/s. and rain rates up to 50 mm/hr.

To the person who…

…told me words don't move mountains

…made me believe I'm my own work

…loved me unconditionally

blessed indeed is the man who hears many gentle voices call him

DAD

Your beloved daughter, Ruba

ACKNOWLEDGMENTS

I would like to thank my advisor, Dr. Linwood Jones and my committee members, Mr. James Johnson, Dr. Takis Kasparis and Dr. Stephan Watson, for their guidance, advice, interest and time. I would like to thank my parents for their love, encouragement and support that carried me through my entire life and made me stronger each day along the way. Also, I am thankful to my team members for their continuous assistance especially Salem El-Nimri, Suleiman Al-Sweiss and Liang Hong.

I want to give my special thanks to Mr. and Mrs. Johnson for their help and tremendous love throughout my graduate school and this project. Last but not least I would like to thank all of my friends for their encouragements.

This work was accomplished with the help of NOAA's through Dr. Peter Black and Mr. Eric Uhlhorn.

TABLE OF CONTENTS

LIST OF FIGURES

LIST OF TABLES

LIST OF SYMBOLS/ACRONYMS

CFRSL   Central Florida Remote Sensing Lab

RadTb   CFRSL Radiative Transfer Model

SFMR   Stepped Frequency Microwave Radiometer

HIRA   Hurricane Imaging Retrieval Algorithm

RTM   Radiative Transfer Model

NASA   National Aeronautics and Space Administration

USSR   Union of Soviet Socialist Republics

ESMR   Electronically Scanning Microwave Radiometer

SMMR   Scanning Multi-Channel Microwave Radiometer

SSM/I   Special Sensor Microwave/ Imager

TMI   TRMM Microwave Imager

SSM/IS   Special Sensor Microwave Imager/Sounder

AMSR   Advanced Microwave Scanning Radiometer

DOD   Department of Defense

SST   Sea Surface Temperature

NOAA   National Oceanic and Atmospheric Administration

HIRad   Hurricane Imaging Radiometer

TRMM   Tropical Rainfall Measuring Mission

TPC/NHC	Tropical Prediction Center/National Hurricane Center
HRD	Hurricane Research Division
TPC	Tropical Prediction Center
HRad	Hurricane forward RTM
AOC	Aircraft Operating Center
UMASS/MIRSL	University of Massachusetts Microwave Remote Sensing Laboratory

CHAPTER 1 INTRODUCTION

The Central Florida Remote Sensing Lab, CFRSL, is engaged in research to improve microwave remote sensing techniques for ocean and atmospheric geophysical parameters, which include the measurement of rain rate over oceans, ocean surface wind speed, and sea surface temperature in hurricanes. Previously, the CFRSL developed an analytical microwave radiative transfer forward model, known as RadTb that was tuned to match satellite passive microwave measurements from the ocean surface [1, 2]. This thesis extends the previous work to consider extreme winds and rain that occur in hurricanes and to develop an inverse geophysical retrieval algorithm for rain rate and surface wind speeds from microwave radiometer measurements in hurricanes.

Chapter 1 provides the description of the thesis objectives and a brief overview of passive microwave remote sensing, which includes a discussion of current airborne and satellite microwave radiometer measurements. Also, the physical characteristics of hurricanes are described. Chapter 2 presents microwave radiative transfer theory for the ocean, discussing both the sea surface and atmospheric emissions. The radiative transfer model for hurricanes is presented in Chapter 3, which includes the present Stepped Frequency Microwave Radiometer (SFMR) geophysical retrieval algorithm and this thesis hurricane imaging rain rate and wind speed retrieval algorithm (HIRA). The validation of the HIRA retrieval algorithm is given in Chapter 4. Finally, conclusions and recommendations for future studies are presented in Chapter 5. Also, appendices are provided to give further information on several related topics along with MATLAB codes developed during this research.

1.1 Thesis Objectives

This thesis deals with the use of microwave remote sensing for hurricane observations and also with the development of a geophysical retrieval algorithm, which has application to airborne microwave remote sensing for improving geophysical parameter observations in hurricanes.

The Central Florida Remote Sensing Lab, CFRSL, is engaged in research to improve the radiative transfer modeling of the microwave brightness temperature of the ocean during a hurricane. For this thesis, the Stepped Frequency Microwave Radiometer, SFMR, rain algorithm is incorporated into the CFRSL forward radiative transfer model (RadTb) and, an inverse radiative transfer model (RTM) geophysical retrieval algorithm (HIRA) is developed to retrieve hurricanes parameters; rain rate and surface wind speed. The algorithm will use airborne multi-frequency, C-band (4 GHz – 7 GHz) brightness temperatures from the SFMR, which views the sea surface at nadir incidence.

Parametric studies are conducted to demonstrate the magnitude of the effects of heavy rain on radiometer observations in hurricanes, and the HIRA will be validated by comparison with SFMR retrievals from various hurricanes in 2003-2005.

1.2 Blackbody Radiation

Over the past several decades, microwave remote sensing has served as an important tool for monitoring the atmospheres and surface of the earth. The term "Microwave Remote Sensing" encompasses the physics of radiowave propagation in and interaction with material media, including surface and volume scattering and emission.

2

The importance of using microwaves in remote sensing lies in their capability to penetrate clouds and to some extent rain. Further, the information available from microwaves is complementary to that available in the visible and infrared regions of the electromagnetic (EM) spectrum.

Remote Sensors are usually divided into two groups according to their operational modes: Active sensors provide their own source of illumination and therefore contain a transmitter and a receiver, and they include various types of radars. On the other hand, passive sensors measure the natural blackbody emissions and therefore are simply receivers that are referred to as radiometers.

In the infrared and microwave portions of the EM spectrum, all matter radiates measurable quantities of electromagnetic energy, and when in thermodynamic equilibrium with the surrounding environment, this matter absorbs and emits equal amounts of energy. A blackbody is an ideal absorber, meaning that it absorbs all of the incident radiation and reflects none. The blackbody emittes energy according to Planck's Law [3] as described in (1.1)

$$S(\lambda) = \frac{2\pi hc^2}{\lambda^5} \frac{1}{e^{ch/\lambda kT} - 1} \, , W/m^2/m \tag{1.1}$$

where h is Planck's constant (6.6253 * 10^{-34} joule-sec), and k is Boltzman's constant (1.38 * 10^{-23} joule/Kelvin), λ is the wavelength in m, T is the temperature in Kelvin and c is the speed of light in m/s.

Figure 1 shows Planck's law on a linear scale. This spectrum is used as a reference against which to compare the radiation spectra of other physical media at the same physical temperature. Most matter does not radiate as efficiently as a blackbody; so

we define the ratio of the observed emission to the theoretical blackbody as the emission efficiency or emissivity (ε). Emissivity varies with the observing wavelength or frequency.
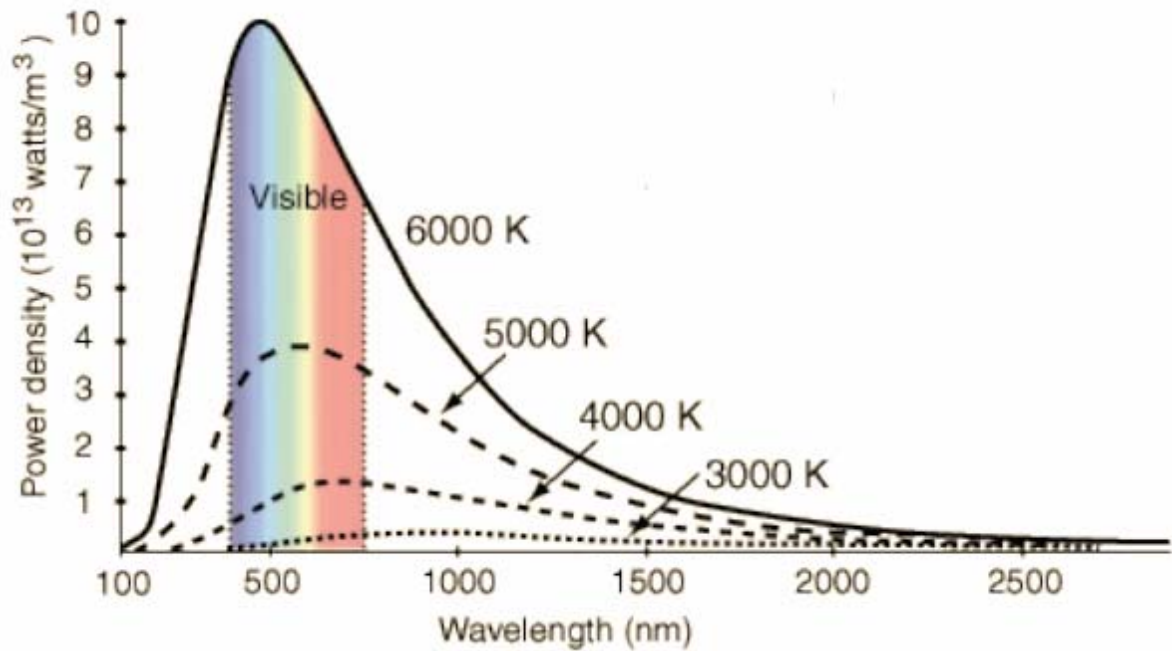
Figure 1 Planck's radiation law for various blackbody physical temperatures.

In the microwave portions of the electromagnetic spectrum, Planck's law simplifies to the Rayleigh-Jeans law. Figure 2 shows log-log plots for both. Over the low-frequency portion of the Planck's emission spectrum, the spectral emittance may be approximated by a straight-line relationship (Rayleigh-Jeans) according to

$$S(\lambda) = \frac{2\pi ckT}{\lambda^4} \qquad W/m^2/m$$

$$= \frac{2\pi kT}{\lambda^2} \qquad W/m^2/Hz$$

(1.2)

since $ch\!\!\big/\!\!_\lambda << kT$. The difference between Planck's law and Rayleigh-Jeans reduces to

less than 1% provided that $f\!\!\big/\!\!_T < 3*10^8 \ Hz/K$.
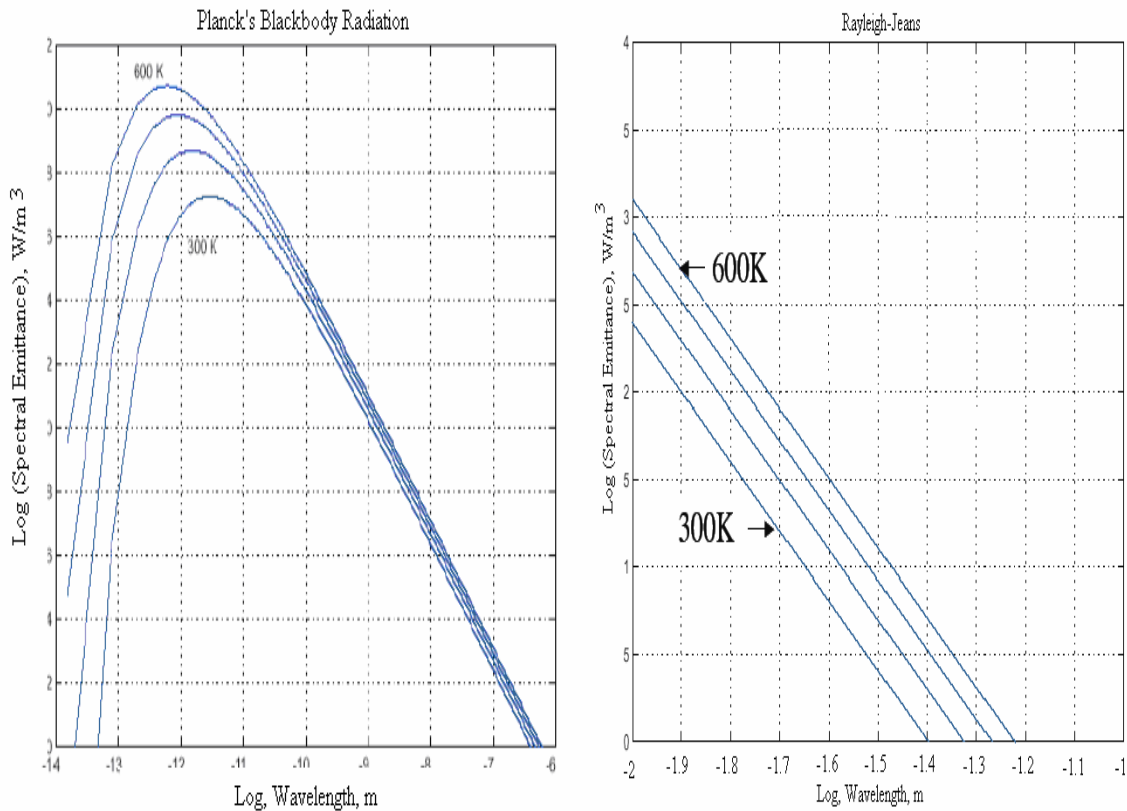
Figure 2 Log-log plots for Planck's law (left panel) and Rayleigh-Jeans approximation (right panel).

Radiative transfer models (RTM's) are analytical models used for calculating the

various sources of EM emissions from physical media. The RTM is important in the field

of remote sensing; and one common application is for geophysical retrieval algorithms.

5

These algorithms use statistical estimation techniques to compare brightness measurements with theoretical calculations from the RTM to determine the most probable environmental conditions that have produced the measurements. Applications for microwave remote sensing include airborne and satellite remote sensing of atmospheric and surface environmental parameters such as atmospheric water vapor and surface temperature for land, ice and water.

1.3   Passive Microwave Remote Sensing

For over 40 years, microwave radiometry has been an integral part of NASA's Earth Observations Program. Satellite microwave remote sensing is a special application of microwave communications technologies for the purpose of collecting geophysical information about targets including objects and media without making physical contact. There is an interaction between propagating electromagnetic waves and matter wherein the environment imposes a modulation on the electromagnetic wave, which becomes its identifying signature. Passive microwave instruments, known as radiometers, fall into three categories; imagers of surface features, surface feature profilers, and sounders of atmospheric profiles of temperature, water vapor and other trace gasses with altitude.

Experience with microwave radiometric data from spacecraft dates back to December, 1962, when the sensors abroad the Mariner 2 spacecraft provided man with the first close observation of the plant Venus [4]. Starting in 1968, microwave radiometers have been used for earth observations aboard several satellites including: Cosmos 384 (USSR); Nimbus 5, 6 and 7; Skylab; TIROS and SeaSat. For example, the

electrically scanning microwave radiometers (ESMR) flown aboard Nimbus 5 and 6 provided the first synoptic images of sea ice in the Antarctic and Arctic regions during the winter season, when visible and infrared sensors do not work well.

Since the 1980's, microwave radiometer imagers (e.g., SMMR, SSM/I, TMI, SSM/IS and AMSR) have routinely operated on NASA research and DOD weather satellites. Multi-frequency microwave imaging of the earth's surface has proven successful because simultaneous brightness temperature (T_b) measurements at different wavelengths and EM polarizations enable simultaneous retrieval of several environmental parameters. Thus, atmospheric, oceanic and fresh and sea ice geophysical parameters are remotely sensed using space-borne multi-frequency microwave radiometry. The radiometer frequencies of interest span the range of 1.4 GHz to approximately 200 GHz. Each radiometer channel (frequency) is selected for its ability to respond significantly to a desired geophysical parameter.

1.4 Oceanic Remote Sensing

The calculation of blackbody microwave emissions from the earth and atmosphere is described by radiation transfer theory, which is illustrated in Fig. 3. The apparent brightness temperature (T_{app}) seen by a microwave radiometer viewing the ocean surface through a slightly absorbing atmosphere is composed of several contributions, namely:

1. T_{UP}, the upwelling atmospheric brightness temperature emitted along the antenna line of sight;

2. T_{refl}, the sum of the downwelling brightness temperature (T_{DOWN}) and the cosmic background (T_{cos}) contribution that is specularly reflected from the sea surface, and

3. T_{sur}, the sea surface brightness temperature.

At the radiometer antenna, these T_b components combine non-coherently (powers add) as given in (1.3).
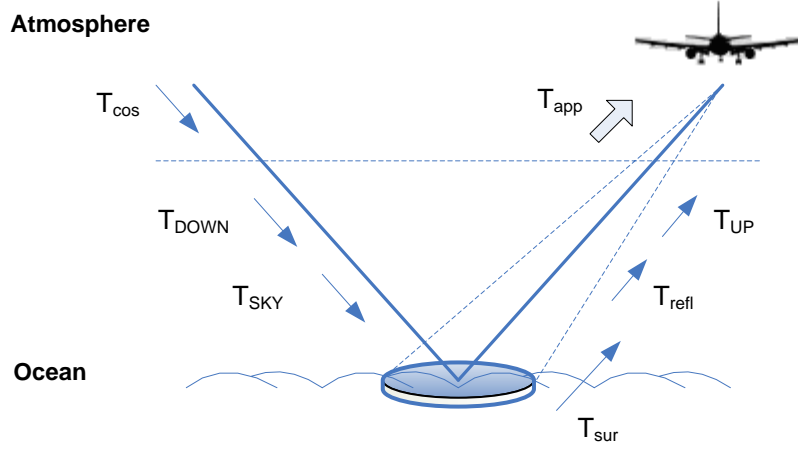
Figure 3 Brightness temperature signal as seen by an airborne radiometer.

$$T_{app} = T_{UP} + e^{-\tau}(T_{sur} + T_{refl}), Kelvin \tag{1.3}$$

where $e^{-\tau}$ is the total one-way atmospheric transmissivity. The ability of a microwave radiometer to make observations of surface characteristics, looking through the atmosphere, depends on atmospheric absorption, which is due to oxygen, water vapor, cloud liquid water and rain in the atmospheric column along the line of sight.

The three components of brightness temperatures shown in Fig. 3 are defined as follows:

$$T_{SKY} = e^{-\tau} * T_{\cos} + T_{DOWN} \qquad (1.4)$$

$$T_{refl} = (1 - \varepsilon) * T_{SKY} \qquad (1.5)$$

$$T_{sur} = \varepsilon * SST \qquad (1.6)$$

where ε is the sea surface emissivity, SST is the sea surface temperature in Kelvin and $T_{\cos} = 2.7$ K is the cosmic microwave background.

1.5   Hurricanes

A hurricane is a severe tropical cyclone that forms in the Atlantic Ocean, Caribbean Sea or eastern Pacific Ocean with sustained surface winds of at least 74 mph. In other tropical oceans, similar cyclones are called typhoons. Tropical cyclones start to form when heat and water vapor are being released into the atmosphere from the ocean surface, making the air above the surface humid and warm. Clouds and rain are then formed from the condensed water vapor rising with the warm air. Heat is released from this condensation, which causes vertical air mass convection and the formation of a surface low-pressure zone. This continuous movement of the upward transfer and release of heat further enhance the convergence of surrounding air toward the growing storm center, which starts to circulate under the influence of the earth's rotation.

1.5.1   Physical Characteristics

As the storm intensifies, a closed air circulation is established counter-clockwise in the Northern hemisphere (clockwise in the Southern hemisphere) that causes the formation of an eye. The eye is the hurricane's relatively calm center and clear area, which is encircled by the eye wall or ring of clouds, heavy rain and the peak surface wind speeds. Beyond this region, the wind speeds decrease approximately exponentially in a radial direction from the hurricane center with hurricane-force winds (74 knts) extending radially to about 50 km (small tropical cyclone) to more than 250 km for a large one. The radial distance over which tropical storm-force winds (45 knts) occurs is even greater, ranging as far out as almost 500 km from the eye of a large hurricane.

Hurricanes are readily observed from space by their eye and distinctive spiral cloud patterns. Geostationary and polar weather satellites with high resolution visible and infrared cameras provide the primary observations. An example of a visible image from a polar-orbiting National Oceanic and Atmospheric Administration (NOAA) weather satellite is shown in Fig. 4.
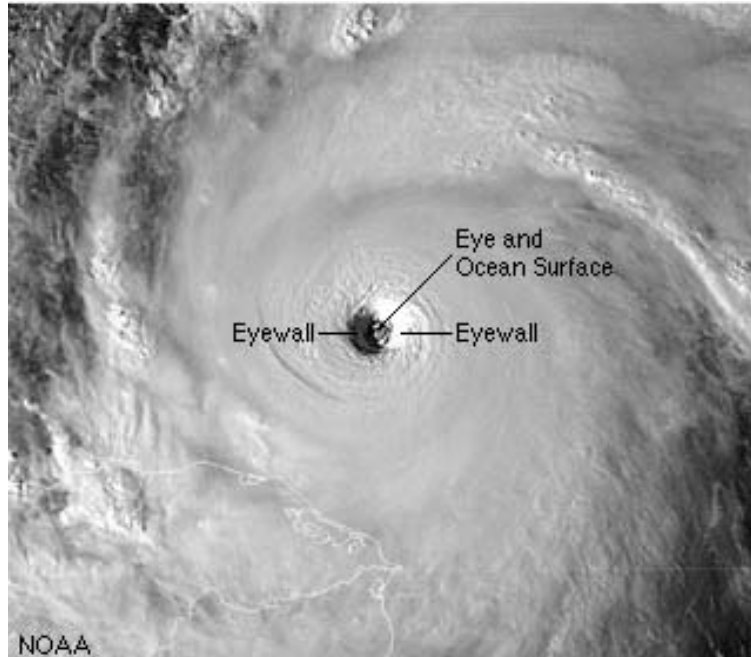
Figure 4 NOAA polar weather satellite visible image of a hurricane.

1.5.2   Importance of Aircraft Hurricane Surveillance

Hurricanes have caused more destruction in the United States than any other type of natural disaster, and according to the NOAA National Hurricane Center, the 2005 season was the worst on record, dating from 1851. Twenty seven tropical storms formed and 15 became hurricanes, breaking the old records of 21 and 12 set in 1933 and 1969, respectively. Seven of the hurricanes developed to category 3 or higher, and for the first time in a single season, three reached category 5 (Katrina, Rita, and Wilma).

The best way to minimize the social and financial impact of hurricanes is through preparedness, which relies on monitoring storms and improved numerical weather forecasting to predict their growth and movement as they develop and make landfall. This is accomplished through a variety of measurement techniques. Primarily

geo-satellites with visible and infrared imagery are used to fix the eye location and make intensity estimates.

Also, when a hurricane is within 24 hrs of making landfall in the continental United States, aircraft flights are made about every 3 hours to geo-locate the eye, measure central pressure, and estimate the maximum sustained surface wind speed. Surface wind estimates are the most important because they are used to forecast the intensity of the hurricane. Aircraft inertial navigation system measurements of flight-level winds are used to estimate the surface wind. Also a few aircraft are equipped with experimental microwave remote sensors (radiometers and radar scatterometers) that can penetrate the heavy cloud cover and weather to make direct measurements of the surface winds. The ability of these remote sensors to make surface wind measurements greatly increases their importance for hurricane monitoring.

1.5.3   SFMR Hurricane Measurements

Because the hurricane warnings are based upon the one-minute max sustained surface wind speed, this measurement is of critical importance to NOAA National Hurricane Center's forecasters. The Stepped Frequency Microwave Radiometer, SFMR, has been making these measurements for many years, flying through storms on the NOAA WP-3 aircraft. The SFMR, was first flown by NOAA in Hurricane Allen in 1980 [5], and subsequently was flown on NOAA WP-3D aircraft through the 1990's developing the ability to infer surface wind speed and rain rate from multi-frequency brightness temperature measurements. Calibration of the SFMR in wind speed by

collocated comparisons to in-situ wind measurements during the 1998, 1999, and 2001 hurricane seasons has established its reliability as a data source for hurricane research [6].

SFMR is a nadir-viewing instrument that measures the microwave brightness temperature, T_b, at six C-band frequencies (4.7 – 7.1 GHz). From these data, surface wind speed and columnar rain rate are simultaneously retrieved using a statistical regression algorithm. In the near future, all NOAA and Air Force "hurricane hunter" aircraft will have SFMR instruments. A description of the SFMR instrument is provided in APPENDIX B.

In the next decade, a new C-band instrument known as the Hurricane Imaging Radiometer, HIRad, may replace the SFMR [7]. HIRad improves over the SFMR by imaging surface wind speed and rain rate over a ± 45° swath, which is equal to twice the aircraft altitude. It will be compatible with high altitude jet aircraft and unpiloted aerial vehicles and even has potential for satellite use. The improved RTM developed during this thesis research will be utilized in the design of the HIRad.

CHAPTER 2 OCEANIC RADIATIVE TRANSFER THEORY

As discussed in Chapter 1, the apparent brightness temperature seen by an airborne radiometer viewing the ocean surface through a slightly absorbing atmosphere is the linear sum of individual contributions from the atmosphere and surface. These contributions are the upwelling brightness, reflected downwelling brightness and surface emissions. This chapter will discuss the emissions from both the sea surface and the atmosphere along with a description of the hurricane radiative transfer model.

2.1   Sea Surface Emissions

The sea surface emissivity must be well known for purposes of retrieving accurate geophysical oceanic parameters from microwave radiometers. As discussed in Chapter 1, emissivity is defined as the ratio of the thermal radiation emitted by a body to that from a perfect blackbody, which is wavelength (frequency) and incidence angle dependent for most materials. Media with emissivities less than unity are frequently called greybodies.

Microwave radiometry refers to the measurement of natural noise (greybody) emissions in the microwave spectral range, and according to the Rayleigh-Jeans law, the radiated energy from the media is proportional to the brightness temperature of the greybody. The greybody power collected by the microwave antenna viewing the ocean surface through a non-attenuating atmosphere is given by (2.1),

$$P_{greybody} = k * T_b * B \tag{2.1}$$

where, $T_b = \varepsilon * T_{phy}$ and T_{phy} is the physical temperature in Kelvin, k is Boltzman's

constant and B is the receiver pre-detection bandwidth over which the power is collected.

2.1.1 Dielectric Constant

Precise knowledge of the sea water complex dielectric constant (also called the

permittivity, e) is required to calculate the microwave radiation emission at the air/sea

interface. This thesis uses the dielectric model of Klein and Swift [8], which describes the

relative dielectric constant with a single Debye relaxation law [9] as

$$e(T,S) = e_\infty + \frac{e_S(T,S) - e_\infty}{1 + \left(i\dfrac{f}{f_R(T,S)}\right)^{1-\eta}} - i\frac{\sigma(T,S)}{(2\pi e_0)f} \tag{2.2}$$

where,

$i = \sqrt{-1}$;

f is the radiation frequency in GHz

$e_S(T,S)$ is the static relative dielectric constant

T is water temperature in Kelvin

S is salinity in parts per thousand

$e_\infty = 4.9$ is the relative dielectric constant at infinite frequencies

$f_R(T,S)$ is the Debye relaxation frequency in GHz

η is the Cole-Cole spread factor, which is set to zero in the Klein-Swift model

$\sigma(T, S)$ is the conductivity of water in Siemens/m, and

e_0 is the vacuum electric permittivity.

The specular ocean surface emissivity is determined by the Fresnel equations, which are functions of dielectric constant. The Fresnel equations for both vertical and horizontal polarization are discussed in the next section.

2.1.2 Fresnel Reflection Coefficient Air to Water

The Fresnel equations given below are used to calculate the electric field (voltage) reflection coefficient at the boundary of two semi-infinite media as shown in Fig. 5 [3]. For the case of an EM wave incident upon the ocean surface, there will be a reflected wave at an angle according to Snell's law and the electric field intensity is given by the Fresnel voltage reflection coefficient times the incident electric field strength. This specular reflection coefficient is a function of the dielectric mismatch of the EM characteristic impedances of air and seawater.
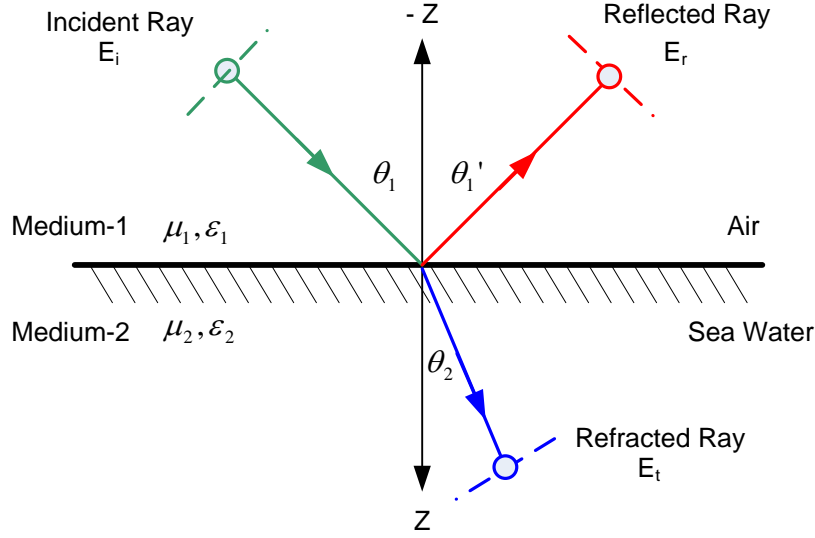
Figure 5 Plane wave electric field (voltage) reflection and transmission at the air/sea interface.

The Fresnel voltage reflection coefficients for both the horizontal and vertical polarizations are given in (2.3) and (2.4) for the special case where medium-1 is air with the relative permittivity, $e_{r1} = 1.0$ and permeability, $\mu_1 = \mu_0$ and medium-2 is sea water with relative permittivity, e_{r2} and permeability, $\mu_2 = \mu_0$

$$\rho_{H-pol} = \left[\frac{\cos\theta_1 - \sqrt{e_{r2} - \sin^2\theta_1}}{\cos\theta_1 + \sqrt{e_{r2} - \sin^2\theta_1}} \right] \tag{2.3}$$

$$\rho_{V-pol} = -\left[\frac{e_{r2}\cos\theta_1 - \sqrt{e_{r2} - \sin^2\theta_1}}{e_{r2}\cos\theta_1 + \sqrt{e_{r2} - \sin^2\theta_1}} \right] \tag{2.4}$$

where e_{r2} is the complex dielectric constant of second media, seawater. The relationship between the incidence and the refraction angles is given by Snell's Law:

$$\frac{\sin\theta_1}{v_1} = \frac{\sin\theta_2}{v_2} \tag{2.5}$$

17

where the EM wave propagation velocity in the media is $v_i = \dfrac{1}{\sqrt{\mu_i\, e_i}}$.

Usually, the quantity of interest for radiometry is the power (energy) reflection coefficient, which can be derived from the Fresnel voltage coefficient as,

$$\Gamma = |\rho|^2 \tag{2.6}$$

It should be noted that the Fresnel equations are bilateral and apply for propagation in either direction such that the incident and reflected waves are interchangeable. However, the internal (ocean) and external (air) reflection coefficients defined in (2.3) and (2.4) are *NOT* equal unless incidence angle adjustments are made according to Snell's law i.e., exchange of θ_1 and θ_2 and e_{r1} and e_{r2}.

2.1.3   Surface Emissivity

Ocean microwave emission is strongly polarized and depends upon the dielectric constant of sea water, which is a function of the geophysical parameters (sea surface temperature and salinity). Surface emissivity also depends on ocean surface roughness, which varies with surface wind speed. Sea water complex dielectric constant also varies with microwave frequency. Typical values of ocean emissivity at nadir (incidence angle equal 0°) vary from 0.3 to 0.7 over the frequency range of 1 GHz to 40 GHz.

The ocean surface brightness is usually described by two orthogonal components of the brightness temperature (vertical and horizontal) collected by the radiometer antenna. The emissivity of the ocean is a measure of the efficiency of transmission of internal blackbody radiation across the air/sea interface as shown in Fig. 6. The

18

transmitted energy (at an incidence angle θ_1) is equal to the internal ocean blackbody emission (incident on the sea water/air interface at an incidence angle θ_2') minus the internal reflection.
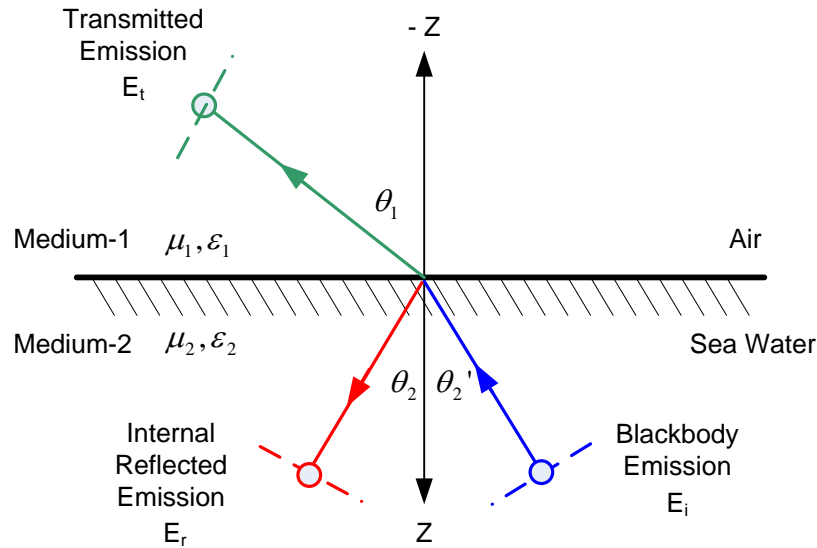
Figure 6 Ocean surface emission is the transmission of the ocean internal blackbody emission through the ocean/air interface.

The usual approach for calculating the ocean emissivity is to recognize that there is equivalence between Fresnel reflection coefficients calculated from air-to-ocean and ocean-to-air, provided that Snell's law is properly taken into account. Specifically, the ocean internal blackbody radiation incident on the boundary at an angle θ_2 crosses the interface at an incidence angle θ_1 in air. Thus the power transmission coefficient ocean-to-air is exactly equal to the transmission coefficient air-to-ocean, provided that the respective incidence and refraction angles are used. The radiometer antenna collects radiation along its line-of-sight, which is at an incidence angle θ_1. The fact that this

19

radiation comes from the ocean internal blackbody radiation at an incidence of θ_2 is not important because this blackbody radiation is isotropic.

Thus, we calculate the ocean emissivity (ε_{ocean}) as

$$\varepsilon_{ocean} = \varepsilon_{smooth} + \varepsilon_{rough}$$

where smooth emission is given by (2.7) using the air-to-ocean Fresnel power reflection coefficient (Γ) and the rough emissivity is wind speed dependent and will be discussed later.

$$\varepsilon = 1 - \Gamma \tag{2.7}$$

Figure 7 shows the magnitude of the power reflection coefficient with respect to incidence angle for sea water in the upper panel and shows the corresponding ocean emissivity in the lower panel.
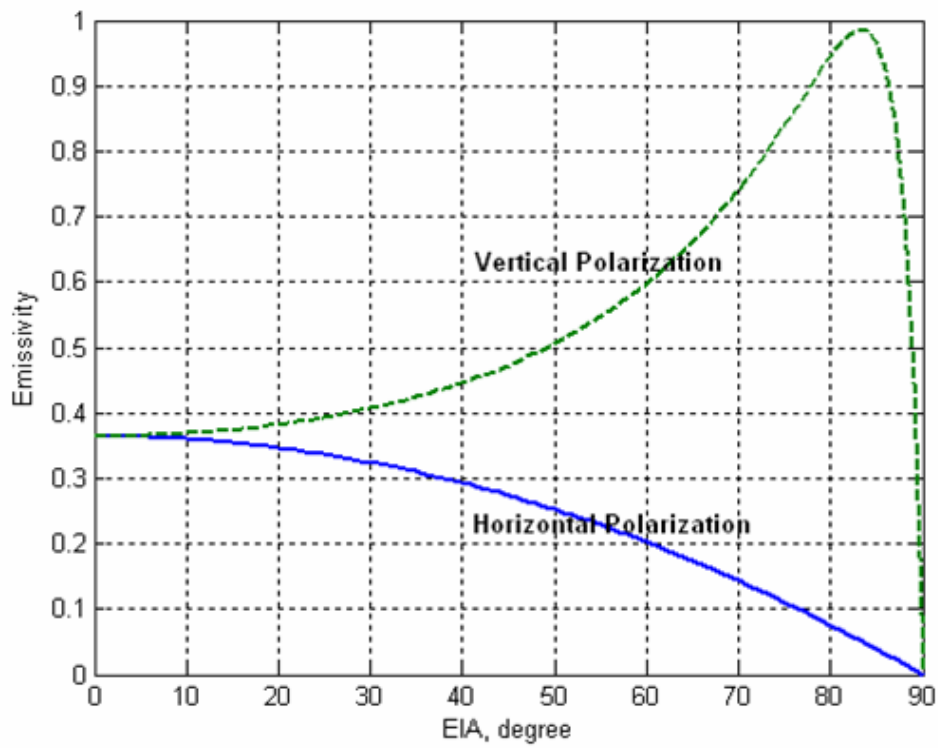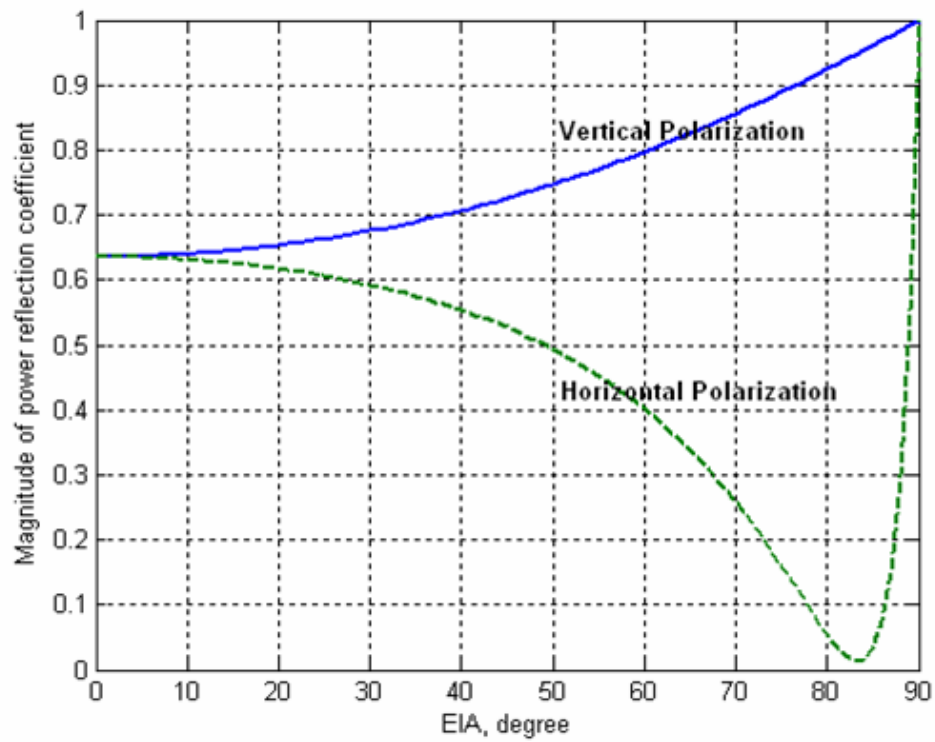
Figure 7 Fresnel power refection coefficient (upper panel) and emissivity (lower panel) for sea water with salinity = 33 ppt and SST = 27.5 C at 4.55 GHz.

Knowing the surface emissivity, both T_{refl} and T_{sur} can be calculated from (1.5) and (1.6), respectively.

2.1.4 Wind Speed Dependence

For realistic wind-roughened ocean surfaces, the microwave emissions depend on both the smooth surface Fresnel power reflection coefficients and the degree of surface roughness. Thus, the specular emissivity is modified by an additive emissivity term to account for roughness effects of ocean waves, which includes the effects of foam produced by the breaking ocean waves. Both the roughness and fractional foam coverage are strongly correlated with the wind shear at the air/sea interface. Figure 8 illustrates the total ocean reflection where the principal component of reflection is specular; but there is also significant diffuse scattering, which has the effect of reducing the power reflection coefficient (increasing the emissivity).
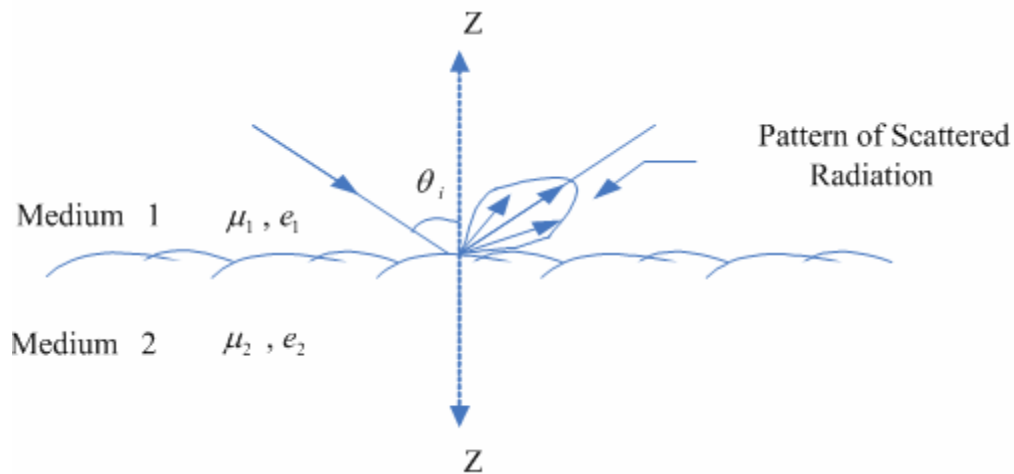
Figure 8 Specular and diffuse reflection from a wind-roughened ocean surface.

22

The source of this ocean roughness is the wind that blows over the sea surface and produces centimeter-length ocean waves. As the wind continues to blow over the sea surface, the energy transfers from short to longer ocean waves and the sea state (large ocean waves) builds. At surface wind speeds of greater than 6 m/s, these gravity waves eventually become too steep and wave breaking occurs to produce "white-caps" and foam.

Rough surface emissivity models depend on the sea surface temperature, frequency, polarization, incidence angle and wind speed. An example of the additive (excess) emissivity versus wind speed from [6] is given in Fig. 9 for SFMR frequencies between 4.5 and 7.2 GHz.
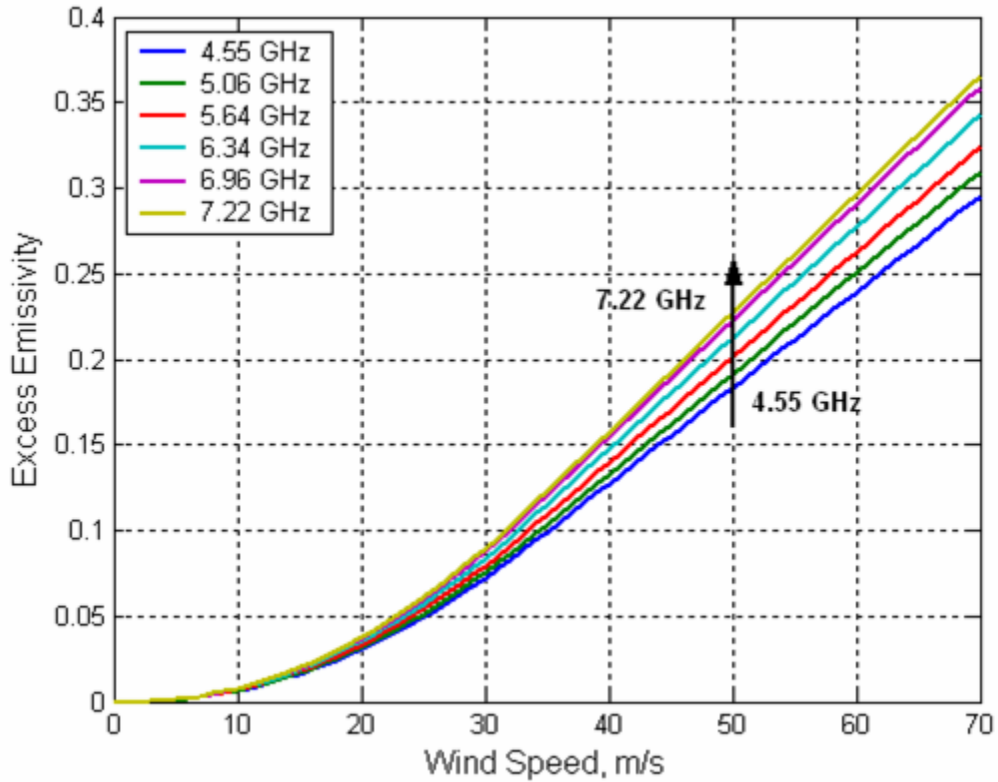
Figure 9 Example of excess ocean emissivity for SFMR frequencies between 4.55 and 7.22 GHz.

2.2 Atmospheric Emissions

The earth's atmosphere plays an important role in microwave radiative transfer and by understanding absorption and emission characteristics of its constituents; certain atmospheric parameters can be monitored. Microwave propagation through the atmosphere is dispersive e.g., in the 1-10 GHz region, the atmosphere is transparent even if clouds and moderate rainfall rates are present, which makes this region suitable for terrain and ocean observations from satellites. In other frequency regions, the resonant absorption due to water vapor (at 22.2 and 183.3 GHz) and oxygen (in the 50~70 GHz

24

and 118.7 GHz), and clouds and rain are important. It is worth mentioning that there is no resonant absorption by hydrometers (cloud water and rain).

The atmospheric microwave brightness temperature is the sum of two components; the upwelling and the reflected downwelling brightness. At microwave wavelengths, for all levels of cloud cover and light to moderate rain rate conditions, the atmosphere may be considered a non-scattering medium, where the apparent brightness temperature representing the downwelling atmospheric radiation is given by [3]

$$T_{DOWN}(\theta) = \sec\theta \int_0^\infty k(z')T(z')e^{-\tau(0,z')\sec\theta} \, dz'$$ (2.8)

where

θ is the zenith (incidence) angle,

$k(z')$ is the total atmospheric absorption coefficient in nepers per unit length at a height z`, which compromises the sum of coefficients for water vapor, cloud liquid water, oxygen and rain.

$T(z')$ is the atmospheric physical temperature at height z',

$\tau(0, z')$ is the optical thickness of the vertical layer between the surface and height z' and is given by [3]

$$\tau(0, z') = \int_0^{z'} k(z)dz \quad , Np$$ (2.9)

and $\sec\theta \, dz$ is the slant path length.

Along the antenna line of sight, the transmissivity of a layer of the atmosphere from the surface to the top of the atmosphere is given by

$$t(0, z') = e^{-\tau(0, z')\sec\theta}$$ (2.10)

For a layered atmosphere (i) defined by the altitude range z_{i-1} to z_i, the transmission coefficient is:

$$t_i = e^{-\tau(z_{i-1}, z_i)\sec\theta}\text{, and}$$

$$\tau(z_{i-1}, z_i) = \int_{z_{i-1}}^{z_i} k(z)dz = \int_{z_{i-1}}^{z_i} k(Z_i)dz = k(Z_i)\int_{z_{i-1}}^{z_i} dz = k(Z_i)\Delta Z_i$$ (2.11)

where

$k(Z_i)$ is the average atmospheric absorption coefficient of the "i^{th}" atmospheric layer in Np/km, evaluated at mid altitude, $Z_i = \dfrac{z_i + z_{i-1}}{2}$ and $\Delta Z_i = z_i - z_{i-1}$ in km

therefore,

$$t_i = e^{-k(Z_i)\Delta Z_i \sec\theta}$$ (2.12)

The total transmission through the atmosphere along the slant path is given by

$$t = \prod_{j=1}^{n} t_j$$ (2.13)

where n is the total number of layers.

The downwelling atmospheric emission from the "i^{th}" atmospheric layer (propagated to the surface of the earth) is

$$T_{DOWNi} = \sec\theta \int_{z_{i-1}}^{z_i} k(z')T(z')e^{-\tau(0,z')\sec\theta}dz'$$

$$= \sec\theta \int_{z_{i-1}}^{z_i} k(Z_i)T(Z_i)e^{-\tau(0,z')\sec\theta}dz'$$

$$= \sec\theta\, k(Z_i)T(Z_i)\int_{z_{i-1}}^{z_i} e^{-\tau(0,z')\sec\theta}dz' = \sec\theta\, k(Z_i)T(Z_i)\prod_{j=1}^{i-1}t_j \int_{z_{i-1}}^{z_i} dz' \qquad (2.14)$$

$$= \left[\sec\theta\, k(Z_i)T(Z_i)\prod_{j=1}^{i-1}t_j\right](z_i - z_{i-1}) = \sec\theta\, k(Z_i)\Delta Z_i T(Z_i)\prod_{j=1}^{i-1}t_j$$

The total downwelling atmospheric emission (at the surface of earth) is

$$T_{DOWN} = \sum_{i=1}^{n} T_{DOWNi} = \sum_{i=1}^{n}\left[e_i T(Z_i)\prod_{j=1}^{i-1}t_j\right] \qquad (2.15)$$

where

$e_i = k(Z_i)\sec\theta\,\Delta Z_i$ is the emissivity of the "i^{th}" atmospheric layer.

As for the total upwelling atmospheric emission, it goes from $i = 1$ to m-layers, where $m<n$ for measurements from aircraft platforms. But for satellite measurements the total atmospheric contributes just like in the downwelling case.

2.2.1   Water Vapor

In the microwave frequency range; there are two resonant absorption lines, 22.2 GHz and 183 GHz, for the water vapor molecule. The absorption (emission) is calculated as a function of altitude using the Van Vleck-Weisskopf model [10] as modified by Gross [11]. In the atmosphere, water vapor density profile is exponential distributed; therefore the major water vapor brightness temperature contribution is for altitudes below 10 km.

The total water vapor absorption coefficient for frequencies below 100 GHz [3] is given by

$$k_{H2O}(f) = k(f,22) + k_r(f) \quad dB/km \tag{2.16}$$

The first element of the total water vapor absorption coefficient, $k(f,22)$, is the absorption coefficient of the 22.2 GHz line, and the second element, $k_r(f)$, is the residual term representing the contributions of all higher-frequencies water vapor absorption lines. The strength of the absorption is governed by; the number of absorbing water vapor molecules per unit volume, the temperature of the gas, and the molecular transitions (allowed energy states) for the water vapor molecule. A plot of the water vapor absorption coefficient as a function of frequency for the US standard atmosphere conditions (T=300 K, and ρ_v=7.5 gm^{-3}) is shown in Fig. 10. Note that the water vapor resonance becomes narrower and its strength increases as the pressure is reduced. This trend continues until the point where the number of water vapor molecules becomes small, and then the attenuation coefficient is dramatically reduced.
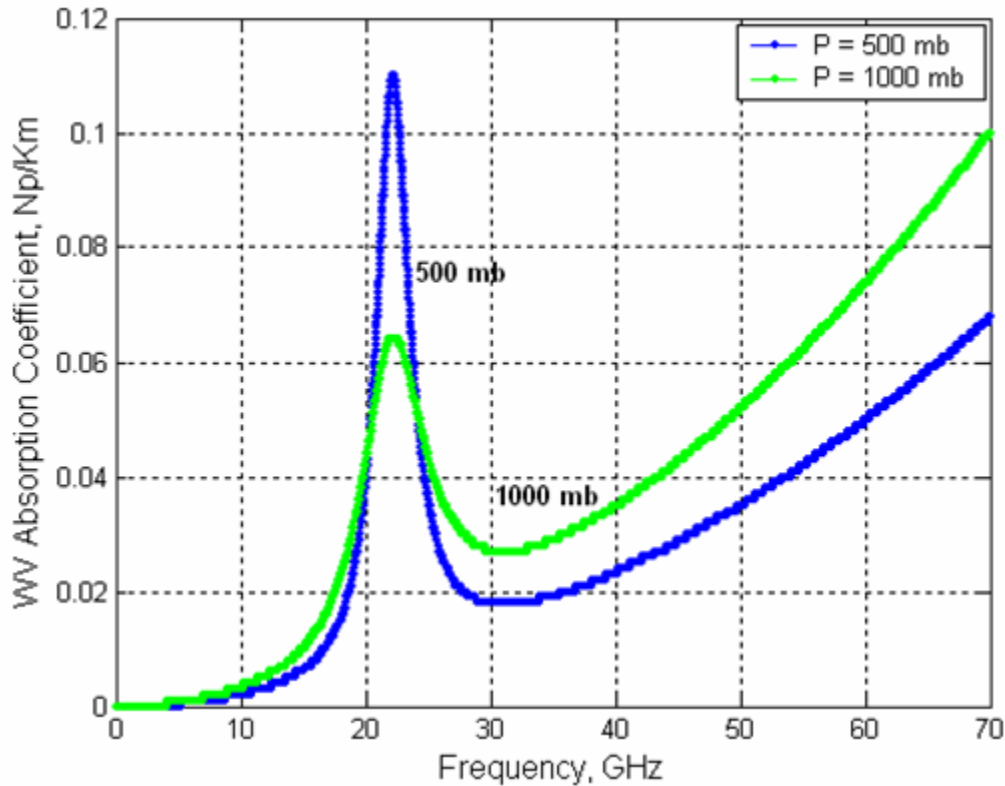
Figure 10 Water vapor absorption coefficient at sea-level (pressure = 1000 mb) and 6 km altitude (pressure = 500 mb).

2.2.2 Oxygen

The microwave absorption (emission) spectrum of oxygen consists of a large number of absorption lines spread over the 50 - 70 GH frequency range and a second harmonic absorption line at 118.75 GHz. At high altitudes, the lines near 60 GHz are closely spaced resonant absorption lines; and near the surface they are merged into a continuum by pressure broadening of the resonant lines. The absorption (emission) is calculated as a function of altitude using the laboratory data of Meeks and Lilly [12] and off-resonance, in the wings of the absorption lines, using the Van Vleck-Weisskopf [10] theory. The strength of the absorption is governed by; the number of absorbing oxygen

29

molecules per unit volume, the temperature of the gas, and the molecular transitions (allowed energy states) for the oxygen molecule. A plot of the oxygen absorption versus frequency is given in Fig. 11.
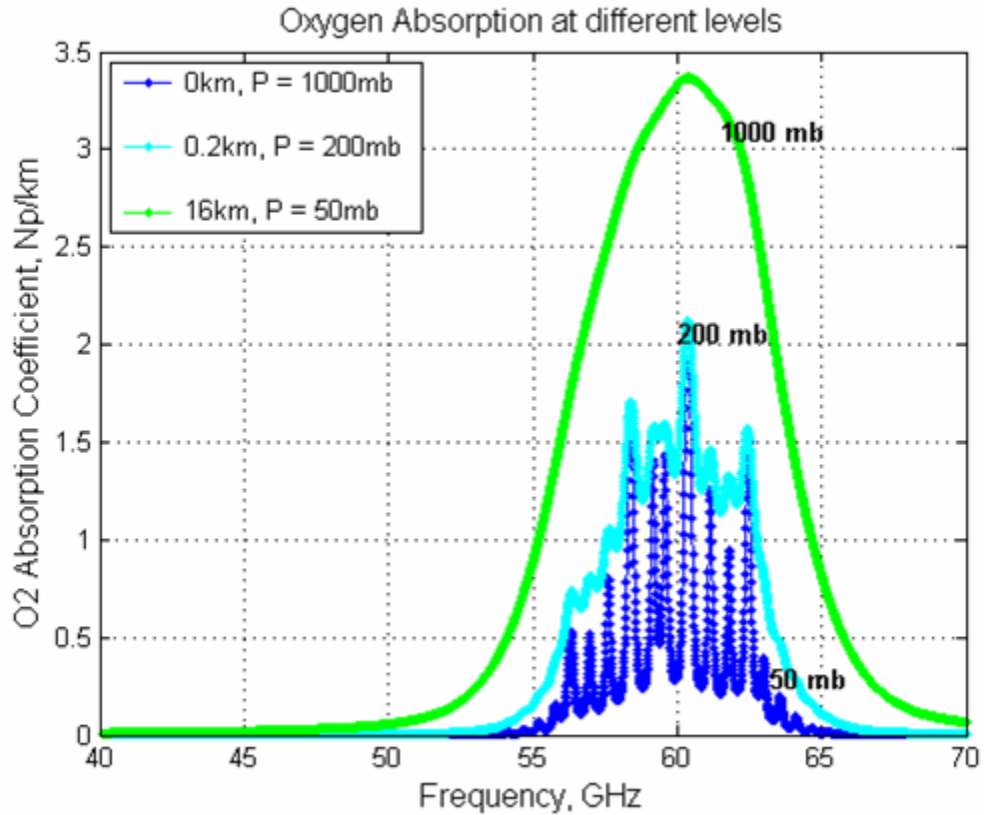
Figure 11 Oxygen absorption coefficients for sea level at different altitudes.

2.2.3   Cloud Liquid Water

In the previous sections, the absorption for clear sky is due to gaseous (molecular) absorption. The interaction of EM waves with particles (e.g., liquid water droplets in clouds and precipitation) in general involves both scattering and absorption. For the

Rayleigh region, the wavelength of the radiation is much greater than the diameter of the water droplets, and here scattering is negligible compared to the effects of absorption, and may be neglected. This is the case for clouds where the drop diameters are less than 100 µm; however, for precipitation where the drop size is of order mm, this approximation does not hold except for the low frequency microwave region less than about 10 GHz.

For the Rayleigh region, the strength of the absorption is proportional to the total mass of the water in the vertical column of atmosphere between the satellite and the surface. Thus, the total mass increases with mean drop size. A plot of the total absorption for typical clouds is given as a function of frequency in Fig. 12.
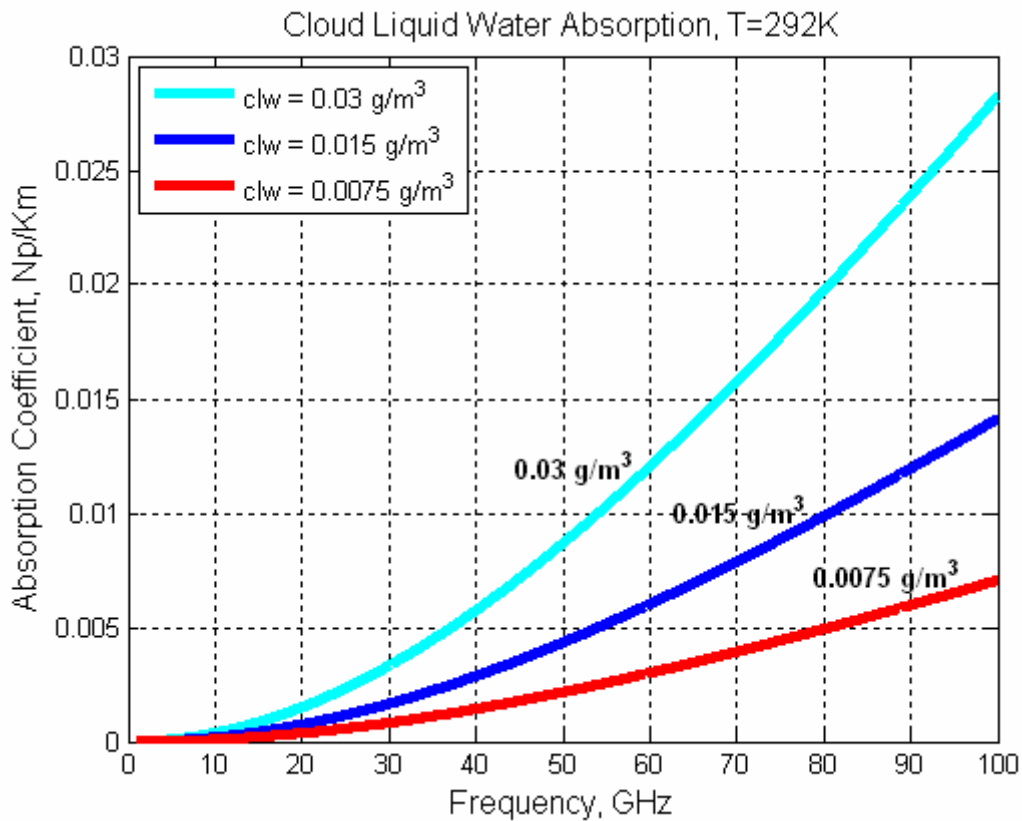
Figure 12 Cloud liquid water absorption for several cloud densities, where the cyan curve is for CLW = 0.03 g/m^3, the blue curve for CLW = 0.015 g/m^3, and the red curve CLW = 0.0075 g/m^3.

2.2.4 Rain

Like clouds, rain over the ocean also increases attenuation in the atmosphere and brightness temperature. The surface contribution in (1.3) will be reduced (attenuated) while the atmospheric emission increases. For heavy rain, the atmosphere can be totally opaque, which masks the surface radiation. For this case, the atmospheric emissivity approaches unity and the brightness temperature saturates at the rain physical temperature ~ 300 K.

The rain model incorporated into the RadTb RTM is a statistical power law regression between absorption coefficient and rain rate derived from the work of Jorgensen and Willis [13] and Olsen et al. [14] of the form

$$k_r = aR^b \tag{2.17}$$

where k_r is the rain absorption coefficient in Np/km and exponent b is 1.15 at low microwave frequencies. The coefficient, a, is given by (2.18)

$$a = gf^{n(R)}$$
$$n \cong 2.6R^{0.0736} \tag{2.18}$$

where 'a' is frequency dependent, which makes the model dispersive and enables the multi-frequency retrieval of rain rate. The constant g equals $1.87*10^{-6}$ Np/km. Figure 13, is a plot of the nadir-viewing absorption coefficient with rain rate for the SFMR frequencies according to (2.17). The relationship between transmissivity, τ_r, and rain absorption coefficient, k_r, at nadir is,

$$\tau_r = \exp(-k_r h) \tag{2.19}$$

where altitude, *h*, is the depth of the rain column (assumed to be the freezing level).
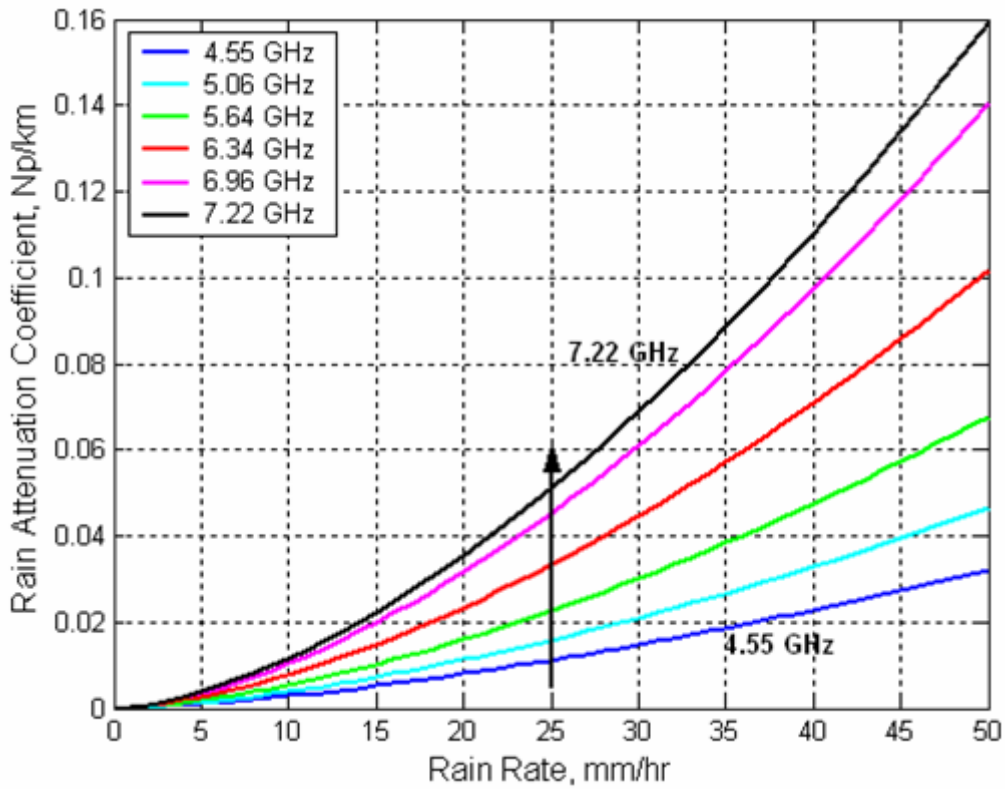
Figure 13 Nadir-viewing rain absorption coefficient for SFMR frequencies.

Figure 14 shows the relation between the transmissivity and rain rate for a rain height of 5 km, which is a typical value over oceans derived from the Tropical Rainfall Measuring Mission (TRMM) Microwave Imager (TMI) [15]. Even at C-band frequencies, the decrease in transmissivity with rain rate is significant when looking

through the entire rain column or at larger incidence angles that result in longer path lengths.
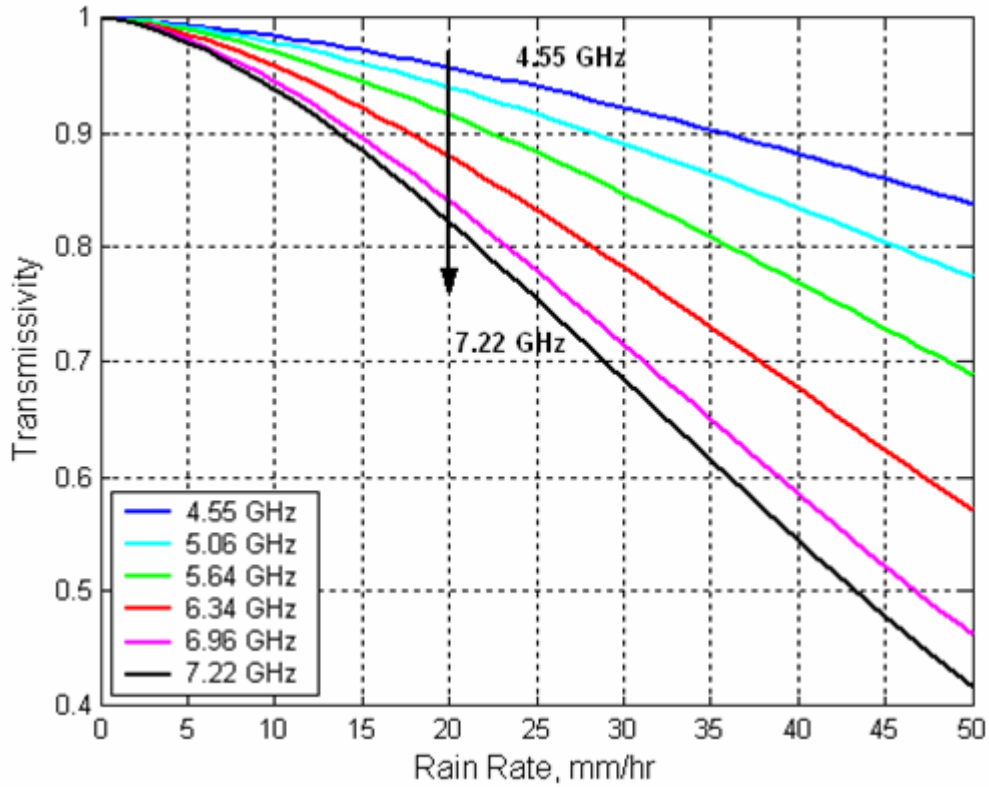
Figure 14 Nadir-viewing rain transmissivity for a typical 5 km rain height.

Table 1 demonstrates the effect of atmospheric absorption on the total apparent brightness temperature, for a wind speed of 20 m/s and a surface water vapor density of 23 gm/m^3, which is typical for a hurricane atmosphere. The table shows brightness temperature contributions for the three terms in (1.3) for moderate atmospheric absorption (i.e., no clouds and medium - heavy rain), and for high absorption (i.e., dense cloud cover and medium - heavy rain). In this example, clouds have a small effect on the

magnitude of the surface contribution and heavy rain has the dominant effect. Moreover, the value of T_{app} for a radiometer operating at 7.22 GHz increases by approximately 50% with heavy rain while the contribution from the surface emission drops from 80% to 33%. Clearly, heavy rain reduces the T_{app} sensitivity to surface emission in hurricanes; and rain through absorption and atmospheric self emission, is dominant in the ocean brightness.

Table 1 Relative contributions to T_{app} at 7.22 GHz

	T_{sur}	T_{refl}	T_{UP}	T_{app}
CLW = 0 gm/cm^2 (No Clouds)				
RR = 10 mm/hr	115.08	11.49	15.49	142.05
RR = 40 mm/hr	72.06	40.28	104.18	216.52
CLW = 0.17 gm/cm^2 (Heavy Clouds)				
RR = 10 mm/hr	113.64	13.07	18.04	144.74
RR = 40 mm/hr	71.16	40.46	106.01	217.62

2.3   Hurricane Radiative Transfer Model

In this section, the atmospheric model for hurricanes will be described; and this will be followed by a discussion of the frequency dispersion of SFMR brightness temperatures with rain. Finally, measured SFMR brightness temperatures will be shown for a typical aircraft pass through the hurricane eye.

Referring to Chapter 1, Fig. 3, there are two atmospheric T_b components and the atmospheric transmissivity, which affect the radiative transfer model. Further, according to (2.8) the upwelling and downwelling atmospheric T_b's are the integral of emissions from each atmospheric layer along the propagation path. The emissivity of each layer is

determined by the sum of the four atmospheric absorption coefficients due to water vapor, molecular oxygen, cloud liquid water and rain.

In hurricanes, the water vapor is high as is the probability for heavy clouds; and both significantly contribute to the absorption; but oxygen does not. Further, rain is the dominant atmospheric absorber; and at high microwave frequencies, where the raindrop diameters become a significant fraction of a free-space wavelength, scattering may be significant. Fortunately at SFMR frequencies scattering is not significant, even for high rain rates.

For RadTb hurricane T_b calculations, the atmospheric profiles of relative humidity and temperature have been defined as a function of radial distance from the hurricane eye by Frank [16]. Cloud cover is variable in hurricanes and surrounding regions, and the most intense rain and deepest cloud cover typically exist in the eyewall region.

2.3.1 Atmospheric Model

RadTb uses a layered atmosphere of 39 layers of 20 km total thickness to describe the atmosphere. At the surface, the thickness of layers is ~ 0.5 km and increases as a function of altitude to account for the fact that the atmospheric density decreases which causes the absorption (emission) to decrease with altitude. RadTb atmospheric subroutines are described in APPENDIX C of this thesis.

A composite hurricane atmospheric model was defined by W. Frank [16]. The model is composed of temperature and humidity profiles for different locations in the

storm. Profiles are defined for the hurricane eye, the eye wall region, and every given 200 km radial distance from the eye. Table 2 is the profile for the eye wall region.

Table 2 Atmospheric model for hurricane eyewall region

Pressure	Height	Temp	Relative Humidity
(mb)	(meters)	(^{o}C)	(%)
1000	0	24.5	95
950	583	23.8	94
900	1,054	21.1	94
850	1,547	18.8	94
800	2,063	16.7	93
700	3,182	11.3	92
600	4,442	5.0	89
500	5,888	-2.3	91
400	7,595	-11.2	85
300	9,682	-24.0	77
250	10,935	-33.3	-----
200	12,396	-46.0	-----
150	14,177	-60.8	-----
100	16,568	-77.1	-----

The temperature profile in Tables 2 shows a freezing height of approximately 5 km which was used as the rain height and the height of the liquid water cloud tops. Given temperature and relative humidity profiles, one can compute the actual water vapor density profile needed for radiative transfer modeling. RadTb assumes that atmospheric water vapor is exponentially distributed with altitude according to,

$$\rho_v(z) = \rho_0 * \exp(-z/H_3), \quad g/m^3 \qquad (2.20)$$

where,

ρ_o is the sea-level water vapor density, g/m^3

z is the geopotential height (altitude) in km

H_3 is the water vapor scale height, km

Therefore, ρ_v must be provided from Table 2 in the form of (2.20).

Relative humidity is defined as,

$$\mathrm{Re}\,lative\ Humidity = \frac{Actual\ Vapor\ Density}{Saturation\ Vapor\ Density} \qquad (2.21)$$

and the saturated vapor density for the temperature profile in Table 2 may be determined from the vapor density/temperature relationship in Fig. 15.
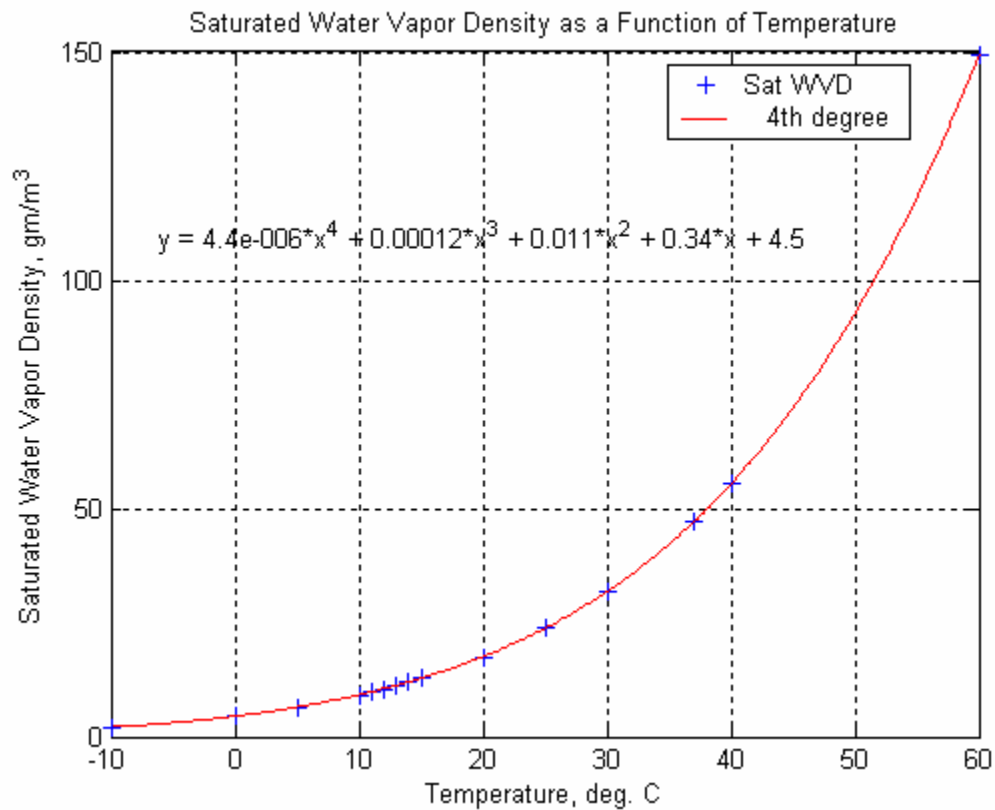
Figure 15 Saturated water vapor density with temperature.

From (2.21), the actual vapor density profile may be determined and, as shown in Fig. 16, an exponential fit can be found to satisfy the form of (2.20). In this case, the best fit to the actual vapor density profile resulted in a value for surface density, ρ_o, of 23 gm/m^3 and a scale height, H_3, of 3.5 km.
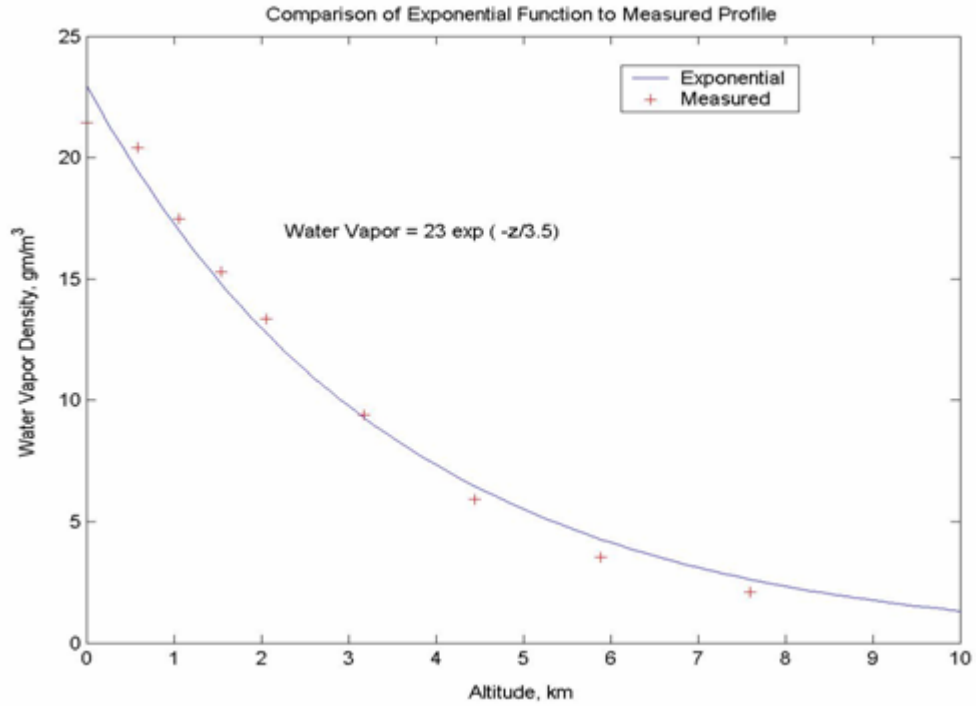
Figure 16 Exponential approximation to water vapor density profile for typical hurricane atmosphere.

This approximation to an exponential function conveniently enables modeling the hurricane atmosphere in a form suitable for RadTb.

A functional relationship for the temperature profile must be defined to complete the hurricane atmosphere definition. Figure 17 shows a linear fit to the temperature data in Table 2 yielding a lapse rate of -4.8 C/km.
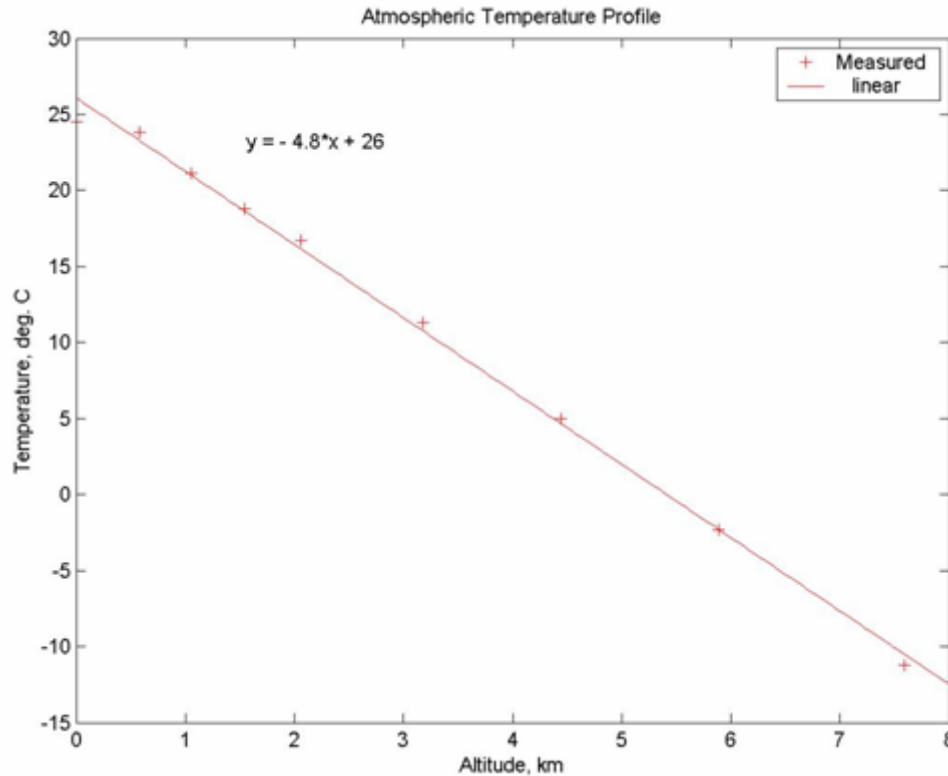
Figure 17 Atmospheric temperature profile for W. Frank composite hurricane model at 0.7 deg. from the eye.

Different temperature and relative humidity profiles are referred to in APPENDIX A for four different cases of the radial distance from the center of the hurricane according to W. Frank composite hurricane atmospheric model.

Rainfall has greater liquid water content distributed among much larger drops than non-raining clouds. The larger size of the raindrops increases their absorption per unit mass and also causes significant scattering that it may no longer be ignored at high microwave frequencies (> 10 GHz). Fortunately, for the long wavelength of the SFMR frequencies, scattering is negligible. Figure 18 shows the results of T_b computations for the SFMR frequency of 6 GHz at rain rates; low (5 mm/hr), medium (20 mm/hr) and high

(40 mm/hr) for a 20 m/s wind speed. Columnar rain rates greater than 40 mm/hr. are routinely experienced in hurricanes resulting in very large increases in observed brightness temperature. The effect of rain is determined by the total rain column, which is estimated to extend to the freezing altitude in convective storms. Therefore, two different freezing levels of 4.25 and 6 km were considered in Figure 18. It is noted that the apparent brightness temperature at SFMR frequencies is quite sensitive to the change of freezing level.
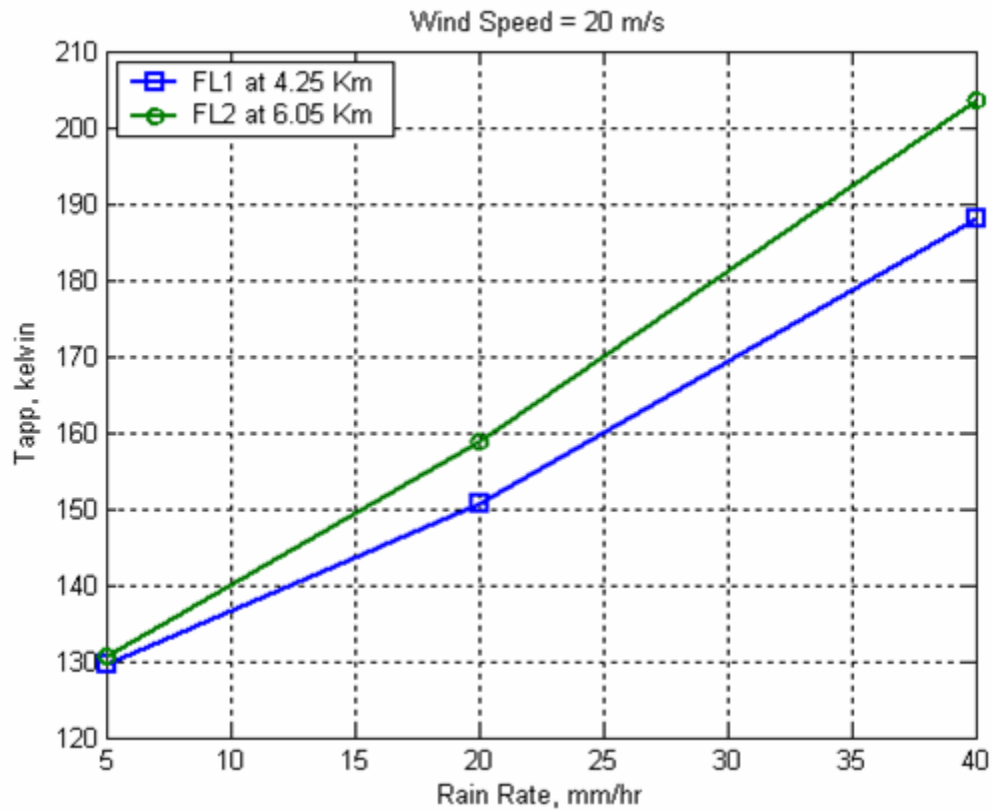
Figure 18 Ocean T_{app} for 6 GHz and two different freezing levels.

An important parameter for rain emission is the rain physical temperature profile. As it falls through the atmosphere, rain equilibrates to the "wet bulb" temperature, which depends on the humidity of the air. Therefore, the humidity profile determines the difference between the wet bulb temperature and the ambient air temperature. The calculation of a wet bulb temperature profile is relatively complicated; therefore, a trade between calculating wet bulb temperature and assuming ambient air temperature for the rain column was performed. The wet bulb temperature at each altitude was calculated from the freezing level to the surface and the T_{app} was calculated over a rainy ocean scene with two different values of surface relative humidity, 40% and 80%. The T_{app} difference between the wet bulb and ambient air temperature is shown in Fig. 19. Over the tropical ocean, the relative humidity is typically 80% or higher [15]. Since the difference in T_{app} for both the dry & wet bulb temperature profiles was less than 2 Kelvin at 80% humidity, which is much less than typical rain T_b contributions, the added complexity in using the wet bulb temperature of the rain is not justified.
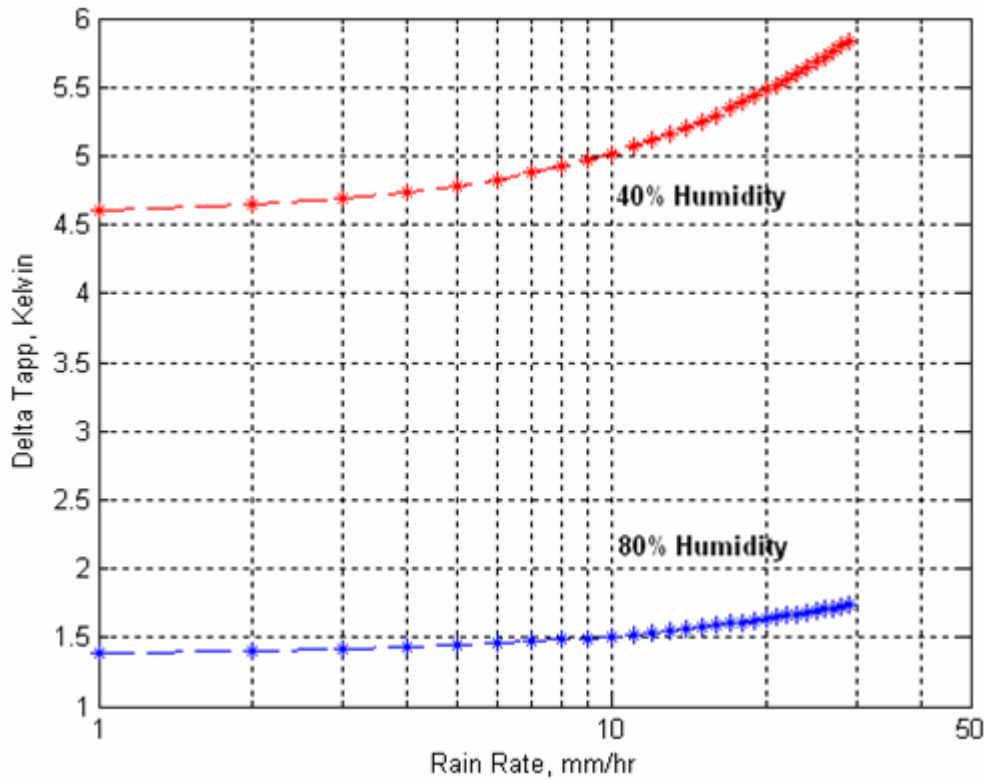
Figure 19 The difference in apparent brightness temperature with respect to rain for two humidity cases.

2.3.2   Frequency Dispersion in Brightness Temperature

Referring to Fig. 9 and Fig. 13 show that both the SFMR wind speed and rain rate models are dispersive with frequency. This provides the ability for simultaneous retrievals. Figure 20 shows two plots of the difference in computed values of T_{app} for the two frequencies 7.22 and 4.55 GHz. Figure 20 (left panel) shows a high sensitivity in dispersion (difference) to variable rain rate, and Fig. 20 (right panel) shows a low sensitivity to wind speed, where rain is not a factor (RR<10 mm/hr). This demonstrates the magnitude of the dispersion involved the fact that simultaneous retrievals depend primarily on the large dispersion with rain rate.

44
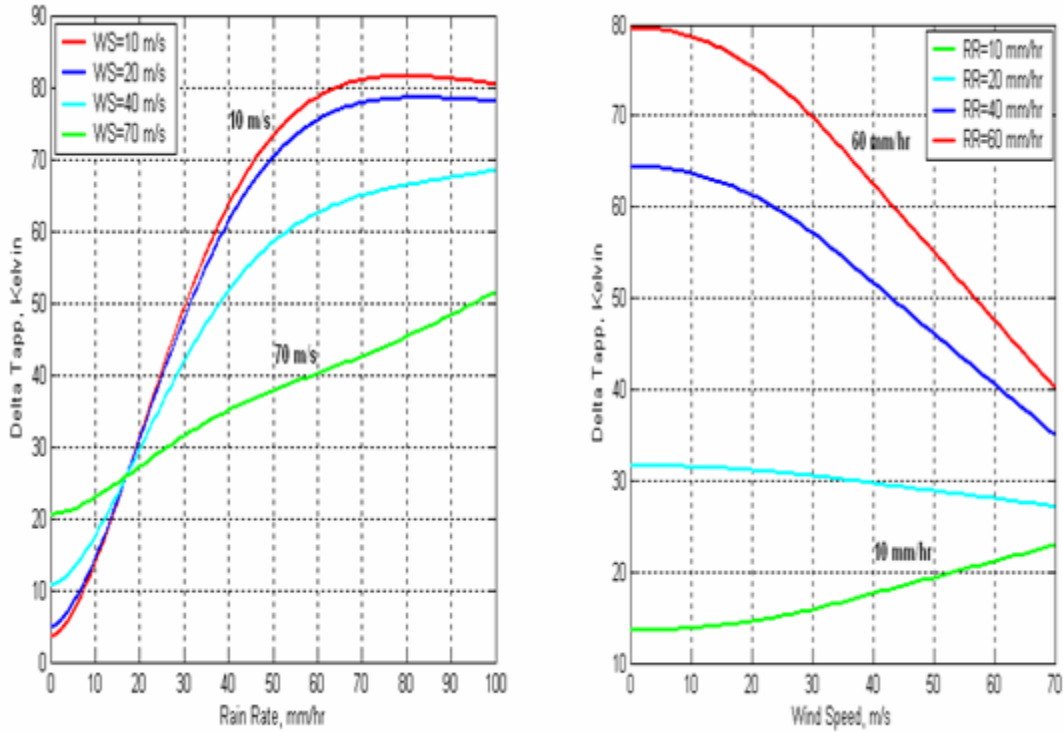
Figure 20 Differential T$_{app}$ for 4.55 and 7.22 GHz for selected wind speed values (left panel) and selected rain rate values (right panel).

A typical pass of the SFMR across the eye of hurricane Katrina 2005 is shown in Fig. 21. This figure shows the time histories of T_b for the six SFMR channels during one pass through the eye of Katrina. Brightness temperatures increase as the aircraft approaches the maximum wind speeds in the eye wall and then decreases rapidly in the calm eye. Upon exiting the eye, a similar pattern is observed where the T_b decreases as the aircraft moves away from the storm.
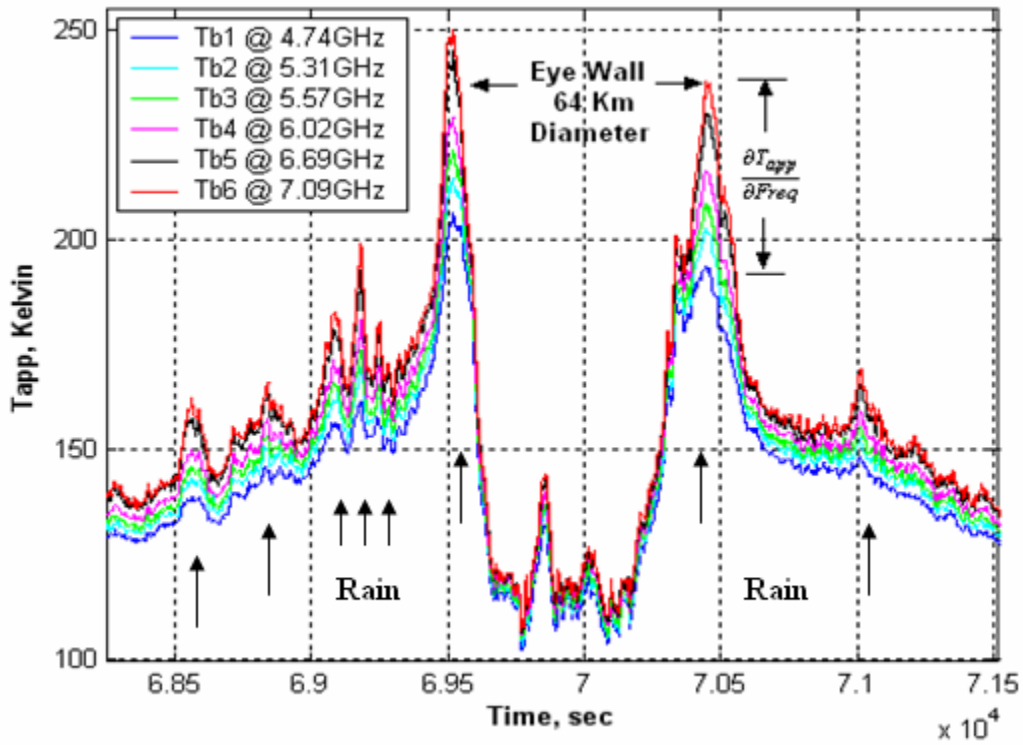
Figure 21 Brightness temperature time series for hurricane Katrina.

The regions of high brightness temperature dispersion outside the center of the storm are associated with rain bands which surround the eye. The spurious brightness temperature spike inside the eye is an aircraft turn and should be ignored.

CHAPTER 3 GEOPHYSICAL RETRIEVAL ALGORITHM

For the past 20 years, surface winds in hurricanes have been estimated remotely using the Stepped Frequency Microwave Radiometer (SFMR) from the NOAA WP-3D aircraft. The first experimental SFMR surface wind measurements were made in Hurricane Allen in 1980 [5], the first real time retrieval of winds on board the aircraft in Hurricane Earl in 1985, and the first operational transmission of winds to TPC/NHC in Hurricane Dennis in 1999. The SFMR is designed for the measurements of the sea surface wind speed and path-integrated rain rate. Since 1999, the HRD has transmitted the real-time SFMR surface winds and rainfall rates to the Tropical Prediction Center (TPC) for application to operational hurricane forecasts.

In this chapter, a review of the present NOAA/SFMR geophysical retrieval algorithm will be given, followed by a discussion of the HIRA retrieval algorithm developed during this thesis research.

3.1   NOAA HRD SFMR Retrieval Algorithm

The SFMR retrieval algorithm [6] is an operational algorithm that provides real time estimates of wind speed and rain rate during hurricane surveillance flights that are telemetered to forecasters at NOAA's Tropical Prediction Center in Miami, Florida. Based upon a statistical regression approach, the algorithm has evolved over the past 20 years of NOAA HRD research flights through numerous hurricanes. Because the algorithm processes SFMR T_b measurements in-flight and in real-time, it uses a priori knowledge of environmental parameters based upon hurricane statistics, such as SST and

humidity and temperature atmospheric profiles. NOAA does not provide post-flight processed data (using improved processing with new input data) for scientific investigation; but the SFMR processed data are generally available upon request for research.

SFMR measures the apparent brightness temperature of an ocean scene below the aircraft that results from primarily the ocean and secondarily the atmosphere emissions. For a constant *SST*, the change in surface emission is directly proportional to the ocean excess emissivity, which is approximately quadratic with wind speed. This SFMR relationship has been derived from statistical regressions of aircraft flight data taken over the past 20 years for wind speeds from ~ 10 m/s to greater than 70 m/s as shown in Chapter 2, Fig. 9.

On the other hand, the atmospheric T_b contribution is primarily due to rain emissivity, which varies exponentially with rain rate and approximately with the square of frequency. The rain rate model is based upon a power law relationship between rain rate and the microwave absorption coefficient (emissivity) of the rain, similar to other models given in [13, 14]. This SFMR model is an empirical relation that has been derived for multi-frequency measurements obtained in SFMR flights [6]. Referring to (2.17) and (2.18), the 'a' coefficient in the rain/absorption coefficient relation is frequency dependant; therefore, the slope of rain absorption coefficient's curves increases with frequency as shown in Chapter 2, Fig. 13. A layered atmosphere of 39 layers of 20 km total thickness is used to describe the atmosphere. This atmospheric model has a priori assumptions about cloud cover and water vapor and air temperature profiles. The transmissivity and absorption per each layer are used to compute brightness temperatures

that corresponded to the downwelling radiation for the atmosphere. Even for fairly low rain rates, the rain is the dominant contributor to the downwelling brightness temperature.

Thus, the retrieval of the surface wind speed and rain rate from a set of T_b's measured at six different frequencies constitutes an inverse problem that generally requires the number of independent measurements to be greater than or equal to the number of parameters retrieved. In particular, SFMR uses a least square method where six measurements are used to infer two parameters (wind speed and integrated rain rate). A forward model relates an "n-length" measurement vector of brightness temperature T_b to an "m-length" vector of retrieved parameters p as,

$$T_{bn} = W_{nm} \times p_m \tag{3.1}$$

where $n = 6$ SFMR frequencies and $m = 2$ parameters.

A linear retrieval is then performed using the partial derivatives of the brightness temperature with respect to the rain rate and surface wind speed parameters as,

$$W_{nm} = \frac{\partial T_n}{\partial p_m} \tag{3.2}$$

The solution for the geophysical parameter estimates is then obtained by taking the sum of square differences of the measured brightness temperature and the modeled brightness temperature according to,

$$\hat{p} = \left(W^T W\right)^{-1} W^T \hat{T} \tag{3.3}$$

The SFMR measures brightness temperatures at a sampling rate of 1 Hz, and usually, a minimum 10 sec average is used in data processing. SFMR T_b data are subject to several quality control procedures to remove measurements within 10 km of land and where aircraft rolls and pitches $> 2^o$, since T_b observations are restricted to normal incidence. Frequently SFMR channels are contaminated by radio frequency interference, RFI, from ground-based sources. Each channel is checked for RFI before solving for wind speed by passing the set of T_b measurements through a median filter. A minimum of two channels are required to solve the system of equations, but the algorithm requires at least three of six, in order to reduce errors.

3.2 HIRA Retrieval Algorithm

In this thesis, a retrieval algorithm known as the Hurricane Imaging Retrieval Algorithm (HIRA) was developed for rain rate and wind speed in hurricanes using SFMR measured brightness temperatures. It is composed of a forward radiative transfer model called HRad, which is a version of RadTb (APPENDIX C), modified especially for hurricane studies, and an inversion algorithm.

HRad uses the atmospheric subroutines in RadTb and outputs absorption coefficients for that layered atmosphere. The absorption coefficients are then fed into a MATLAB program that computes an additional absorption coefficient due to rain and then calculates the three components of the apparent brightness temperature, mainly; the upwelling brightness, the reflected downwelling brightness and the surface emissions

shown in Fig. 3. The inversion algorithm is a least square minimization of differences between computed brightness temperatures from HRad, and measurements from SFMR over wind speed and rain rate ranges of 0~100 m/s and 0~100 mm/hr respectively. A more detailed description of the retrieval process follows.

The HRad algorithm block diagram is illustrated in Fig. 22. The block diagram is divided into a part computed using a FORTRAN program (RadTb) and a second part implemented in a MATLAB code. RadTb uses a layered model of 39 layers of 20 km total thickness to describe the atmosphere. The thickness of layers increases as a function of altitude. Geophysical inputs, described in APPENDIX C, are part of the FORTRAN cycle that calculates three absorption coefficients due to water vapor, oxygen and cloud liquid water. The significant most environmental parameters, which are input to RadTb, are the temperature and water vapor profiles. A definition of the clouds in terms of cloud depth and integrated cloud liquid water is also an input into the layered atmosphere but absorption due to oxygen is relatively insignificant in the hurricane atmosphere.

The absorption coefficients due to water vapor, cloud liquid water and oxygen are then calculated using three different FORTRAN subroutines as shown in Fig. 22; ABSH2O, ACLOUD and ABSO2. The ARAIN subroutine calculates the absorption coefficient of rain according to the power law relation given by (2.17), and the output parameters, K_{H2O}, K_{CLD}, K_{O2} and K_r, are the absorption coefficients in a layered format. The summed absorption coefficients are used as input to the Atmospheric T_{UP}/T_{DOWN} model. The Atmospheric T_{UP}/T_{DOWN} model calculates the loss (transmission coefficient) and self–emission (upwelling and downwelling brightness temperature) of the atmosphere. The entire atmosphere is considered in the downwelling T_b component of the

radiation while only part of the atmosphere between the aircraft and the surface is considered in the upwelling T_b component.
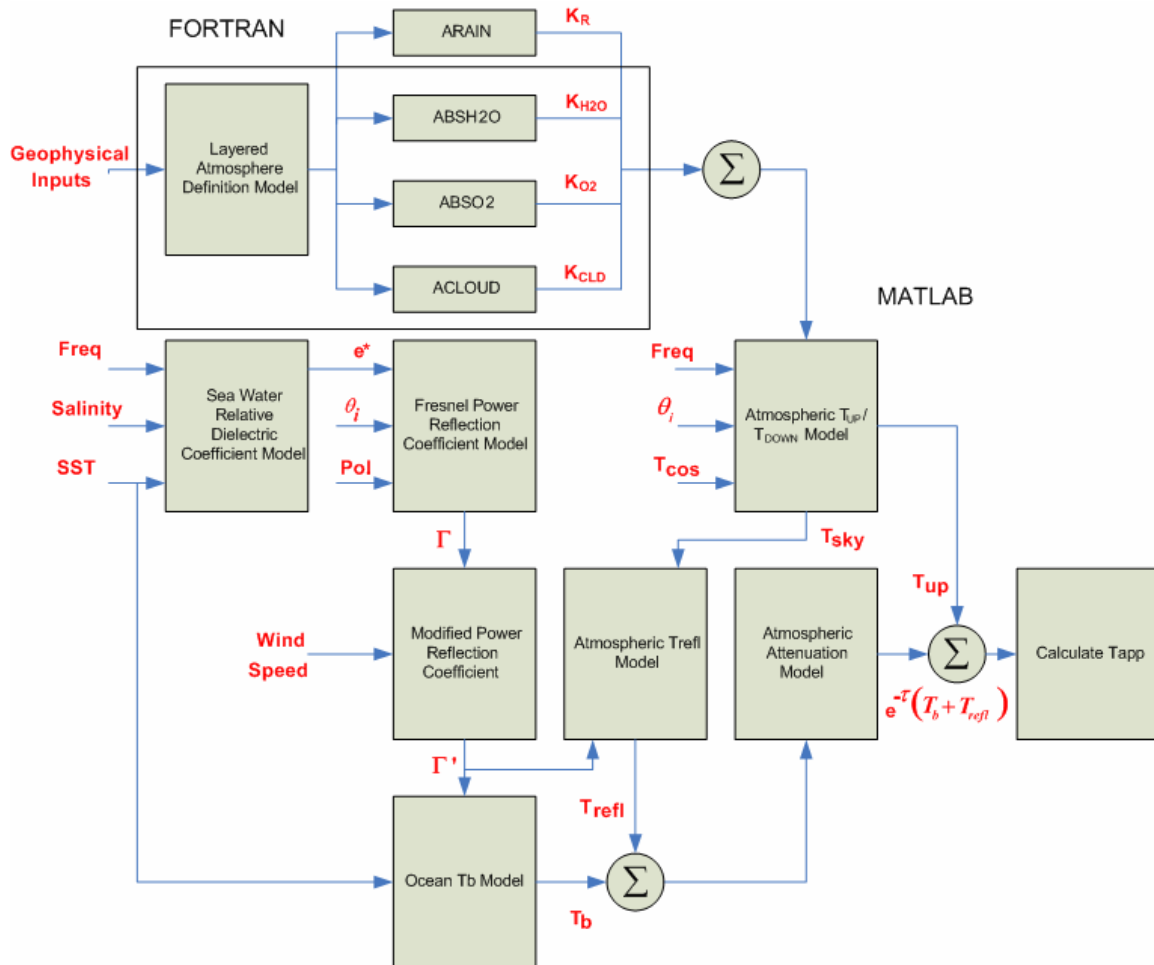
Figure 22 HRad, forward radiative transfer model.

The surface characteristics must be computed to determine the reflected T_{SKY} and the surface emission terms in (1.3). The dielectric constant is computed using the Kline/Swift model [8] and used in the Fresnel power reflection coefficient calculation. The NOAA SFMR wind speed model is used to compute a modified reflection

coefficient as a function of wind speed that determines the reflected T_{SKY} and the surface emission contributions. Finally, these two quantities are attenuated and added to the upwelling radiation term. This produces one modeled brightness temperature value for one frequency, one wind speed value and one rain rate value.

The modeled brightness temperature (T_{app}) from HRad at each of the six SFMR frequencies are placed into a two dimensional matrix for each frequency with wind speed and rain rate as variables. Wind speed is varied in 0.1 m/s steps from 0~100 m/s and rain rate in 0.1 mm/hr steps from 0~100 mm/hr to form a brightness temperature matrix of 10^6 elements for each frequency. This matrix is essentially a table of values that remains fixed for each retrieval that is performed. The table doesn't change unless one of the geophysical input quantities, such as sea surface temperature or water vapor density, is changed. In this sense, HRad is currently a static model rather than a dynamic model able to accommodate variable sea surface temperature, for example, as part of a retrieval.

The HRad matrix is compared with the SFMR measured brightness temperatures, as shown in the block diagram of Fig. 23. SFMR data records contain six brightness temperature time series, sampled at 1 Hz, for an entire flight which might last approximately 3 hours. Each of six SFMR $\hat{T}_b$ vectors in Fig. 23 is made up of one of these 6 time series and compared to every value in each of the six HRad matrices, forming six difference matrices. Each element in these is squared and the algorithm searches for the minimum sum, over all frequencies, of squared difference. The solution is the estimate of wind speed and rain rate corresponding to the given SFMR brightness temperature.
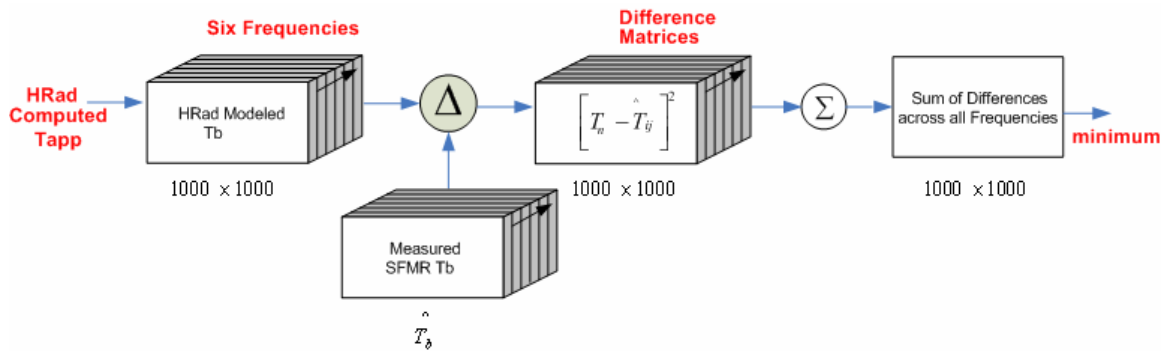
Figure 23 Inversion algorithm.

In Fig. 23, T_n is a 6-element SFMR measurement (T_{app}) vector and $\hat{T}_{ij}$ is the matrix of modeled brightness temperatures. After summing the square difference matrices for all six frequencies, a new matrix is generated and a minimum value was obtained out from it.

Wind speed and rain rate retrievals were obtained from several hurricanes between 2003 and 2005. Figure 24 is a typical example of a retrieved set of wind speed and rain rate for Hurricane Katrina for one of the total five passes through the eye of the hurricane. The data record of 1 sec samples of brightness temperature have been smoothed using a triangular window and a 41 sec running average. The green curve is the retrieved wind speed while the blue curve refers to the retrieved rain rate. The radial distance from the eye is shown at the bottom of the figure. In the eye wall region, maximum absorption and brightness temperatures are achieved that corresponds to the maximum retrieved wind speed and rain rate. Intense rain cells can also be seen outside

the eye wall region. A maximum wind speed of 70 m/s and rain rate above 40 mm/hr were observed in the eye wall.
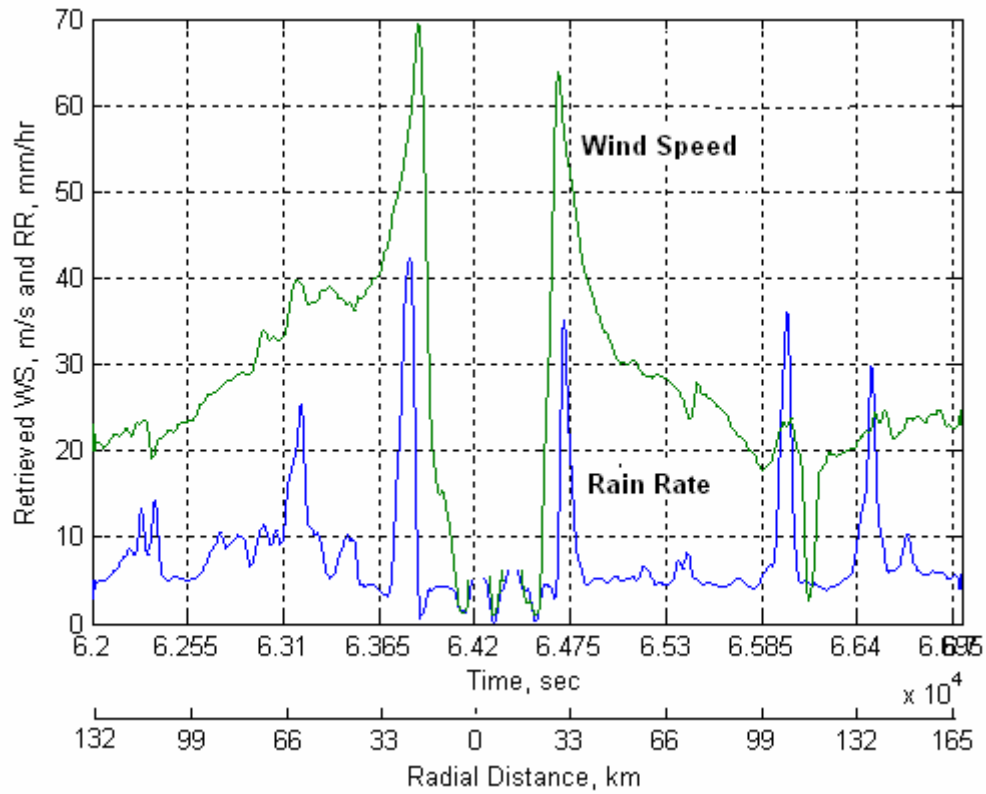
Figure 24 Hurricane Katrina retrieved wind speed, m/s and rain rate, mm/hr.

The HIRA retrieved set of wind speed and rain rate will be compared with NOAA/SFMR retrievals in the next chapter for several hurricanes in 2004 and 2005.

CHAPTER 4 HIRA RETRIEVAL ALGORITHM VALIDATIONS

Validations of the HIRA algorithm will be discussed in this chapter for wind speed and rain rate separately and both will be compared to SFMR data in hurricanes as part of the validation for the algorithm.

A total of five hurricanes from different years are selected. Hurricanes Katrina, Rita and Ophelia were recent 2005 hurricanes and Hurricane Frances (2004) and Fabian (2003) were the selected cases. The complete data set consists of multiple aircraft passes through each of these hurricanes. Since the SFMR was used for model development and these comparisons, the validation part of the SFMR itself will be first discussed.

4.1   NOAA SFMR Wind Speed & Rain Rate Retrieval Algorithm Validation

The NOAA SFMR wind speed and rain rate algorithms have been derived from aircraft flight data taken from the past 20 years [6]. Its accuracy has been demonstrated for wind speed above 10 m/s to greater than 70 m/s, and this is the highest wind speed ever measured by a remote sensing instrument. Initially, the relationship between the emissivity and the surface winds was developed through aircraft missions in which brightness temperature measurements were made by two aircrafts, one operating at higher altitude making SFMR measurements and the other at lower altitude (0.5 km) making in situ measurements of winds. Currently, the NOAA WP-3D aircraft routinely deploys GPS dropwindsondes measuring horizontal wind vector profiles at ~5 m vertical resolution. Estimates of wind at 10 m height above the surface are extrapolated from

mean boundary layer wind measurements by the dropwindsondes. A total of 76 paired samples of SFMR and dropwindsondes from 1998, 1999 and 2001 were used for wind speed algorithm validation. These paired observations were quality controlled to be within 15 km total distance of each other and within 10 km radially with respect to the storm center. All measurements were over open-ocean and the sample was well distributed among storm quadrants and over storm wind strength. In the final result, the mean difference between the GPS measured wind and the SFMR retrieved wind was 1.67 m/s with a standard deviation of 3.29 m/s. The current SFMR ocean emissivity model, shown in Fig. 9, clearly shows that the SFMR T_b's are still increasing at wind speed greater than 70 m/s.

NOAA SFMR rain rate retrieval validation in tropical cyclones was previously performed by comparing to rain rate inferred from the lower fuselage (LF) radar and the tail (TA) radar on board of the NOAA WP-3D aircraft. The collected data for comparisons came from Hurricane Bonnie (1998) and Hurricane Humberto (2001) with a total of 820 paired samples. Relative to radar rainfall estimates, the SFMR 10 sec average path-integrated rain rates were found to overestimate in light rain and an underestimate in heavy rain [17]. A bias of 5 mm/hr of the SFMR rainfall estimate was found compared to the radars.

A constant atmospheric structure is assumed a priori for use during the course of a flight. Input to the radiative transfer model is the Jordan [18] mean hurricane season West Indies sounding (temperature, pressure, and relative humidity as functions of altitude). Output is the atmospheric transmissivity at each of the operating frequencies of the SFMR, from which a linear dependence of transmissivity on frequency is approximated.

NOAA SFMR retrievals assume that there is no cloud cover, which obviously is not accurate; however, the effect of clouds is negligible in the presence of rain. Never the less, this could contribute to the cause of the small rain rate bias. Also an assumed *SST* of 28° C and a salinity value of 36 ppt are generally used. Sensitivity studies were conducted and showed small errors due to making these assumptions [6].

4.2   HIRA Hurricane Comparisons with NOAA SFMR

HIRA wind speed and rain rate retrievals were compared to the NOAA SFMR algorithm results for several hurricanes between 2003 ~ 2005. Results from Hurricane Katrina were the most interesting because there was excellent SFMR data available in near category-5 conditions where ~ 70 m/sec winds were retrieved. A comparison of the HIRA retrievals with corresponding NOAA SFMR results are shown in Fig. 25. The agreement in both wind speed and rain rate for the first pass is quite good, which gives confidence in the HIRA algorithm and the methods being used in modeling and retrievals. Since both HIRA and NOAA SFMR use the same SFMR emissivity model, it is expected that the retrievals should be in reasonable agreement. Never the less, there are significant differences in the retrieval methodology which are necessary to validate.
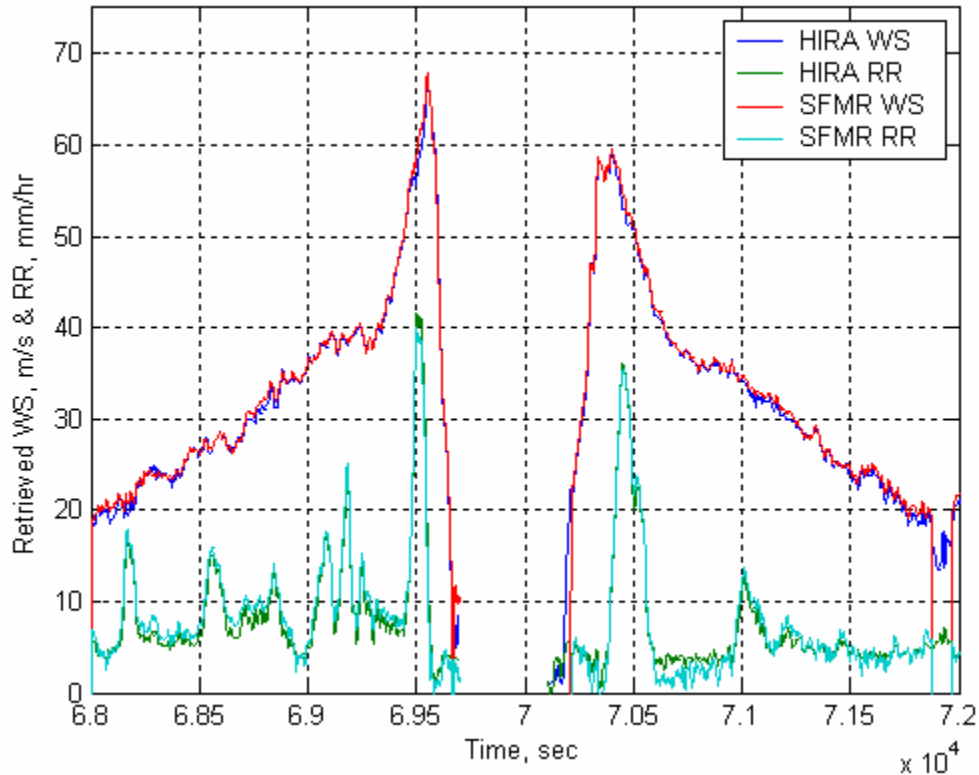
Figure 25 Comparison between SFMR and HIRA retrieved WS and RR for Hurricane Katrina 2nd pass on August 28th, 2005.

Other passes through the eye of Katrina show very similar results and equally good agreement with SFMR. Data from hurricanes Fabian (2003), Frances (2004), and Rita (2005) have been processed, and have all determined the reliability in agreement between HIRA and NOAA SFMR retrievals. Figure 26 shows how well both HIRA and SFMR retrieved wind speed values agree with one another in terms of how well the data is distributed along with the 45 degrees for the whole flight line with a mean difference of 0.95 and a standard deviation difference of 1.3. The same thing applies to rain rate with a difference mean value of 0.53 standard deviation difference of 1.58 as shown in Fig. 27.
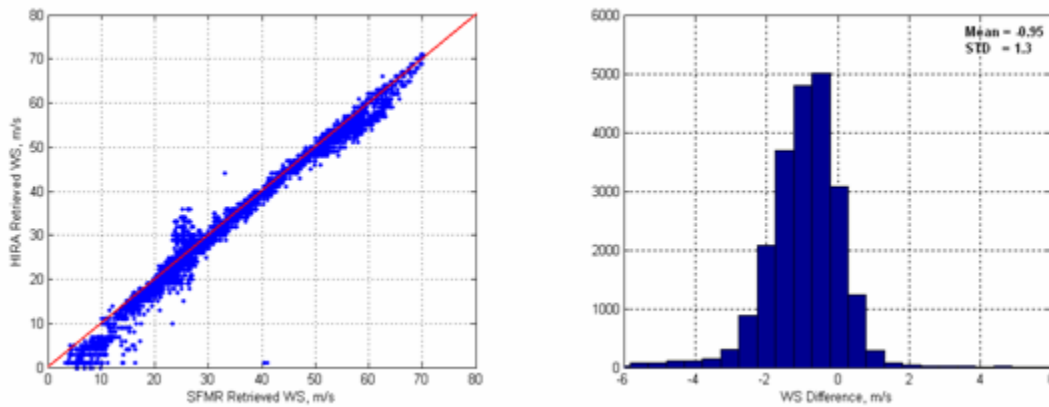
Figure 26 Scatter plot for HIRA and SFMR retrieved wind speed values, m/s and the associated histogram for the difference.
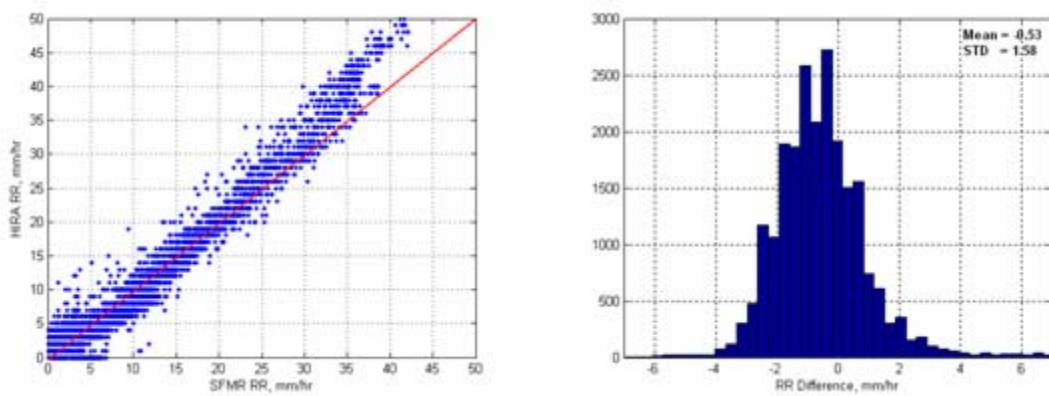
Figure 27 Scatter plot for HIRA and SFMR retrieved rain rate values, mm/hr and the associated histogram for the difference.

There are some differences between the SFMR and the HIRA approaches to solve for wind speed and rain rate retrievals. In this comparison HIRA retrieval algorithm searches for the wind speed and rain rate values that give the minimum difference within a 2D matrix. The SFMR retrieval algorithm described in Chapter 3 runs a forward model and performs a linear retrieval using the partial derivatives of the brightness temperature

with respect to the atmospheric and surface geophysical parameters. Since the HIRA algorithm is physics based, it can be extrapolated to cover different instrument and measurement conditions, such as polarization and earth incidence angle, EIA.

4.3   HIRA Sensitivity Studies

Certain assumptions and approximations have been made in both the SFMR and the HIRA algorithms. The SFMR uses a tropical atmosphere averaged over the hurricane season, whereas HIRA uses a composite hurricane atmosphere characterized as a function of distance from the eye. Also, SFMR does not model clouds and both algorithms assume that the rain temperature is the ambient air temperature. HIRA studies have demonstrated that in the tropics the ambient temperature and rain temperature are approximately equal. Sensitivities to freezing level and the assumption that the rain is uniform with altitude have been demonstrated in the SFMR rain rate validation studies [17]. Sensitivities to selected modeling parameters, assumptions, and approximations have been studied in HIRA retrievals.

After validating the HIRA algorithm, sensitivity studies were conducted to test the performance of the algorithm and to better know how changing some variables in the atmosphere will affect the HIRA retrievals. Hurricane Katrina was picked for these studies. This section will present three different sensitivity studies; *SST*, freezing level and *WV*.

4.3.1 Sea Surface Temperature

The assumed value of *SST* used in Katrina retrievals was 28° C, this was the reference value used in the *SST* sensitivity analysis. In this study, the *SST* was varied between 20 and 32° C in one degree steps, and the retrieved wind speed (*WS*) and rain rate (*RR)* values were computed for each case. Figure 28 is an example of the results that shows the time series of the difference between the HIRA retrieved *WS* values assuming the "correct" 28° C value and retrievals assuming the 22° C case. The largest error in Fig. 28 occurs inside the hurricane eye and is anomalous response not associated with estimating wind speed.
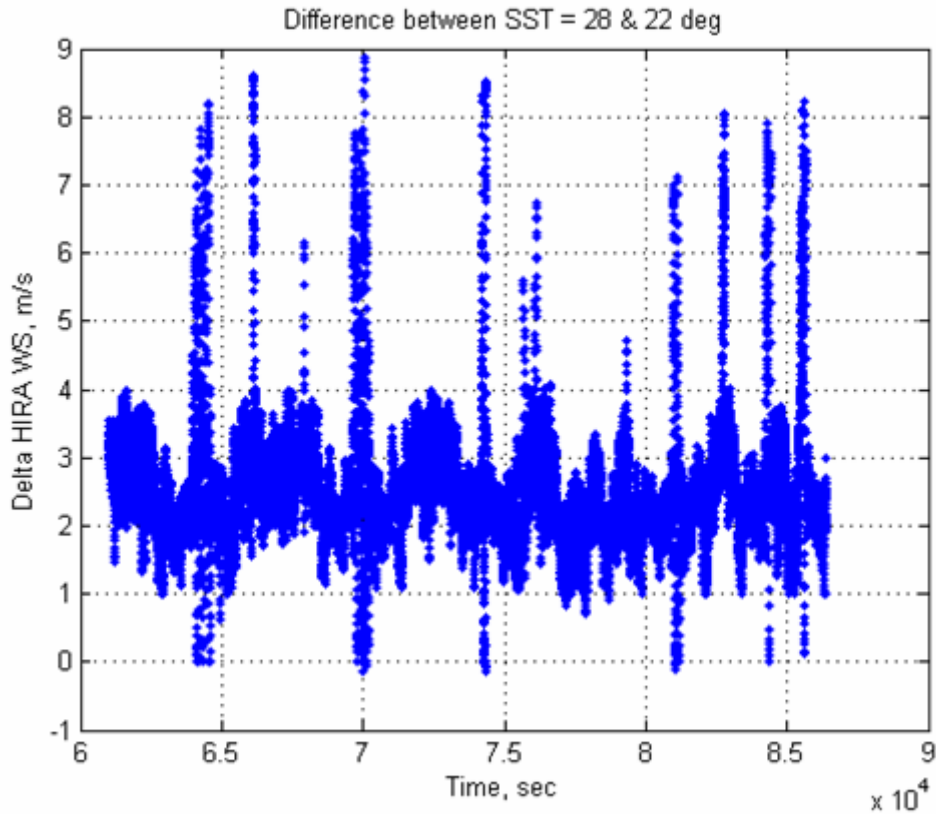
Figure 28 Delta HIRA retrieved WS values as a time series between SST =28 and 22ᵒC.

Figure 29 shows the histogram of the difference between the HIRA retrieved *WS* values for 28° C and 22° C. The mean difference is 2.5 m/s with a standard deviation in the difference of 0.98 m/s. This translates to a mean error of ~ 0.4 m/s per deg C. However, this is for the entire flight and not an error in just estimating maximum wind speed in the eye wall region, for example.
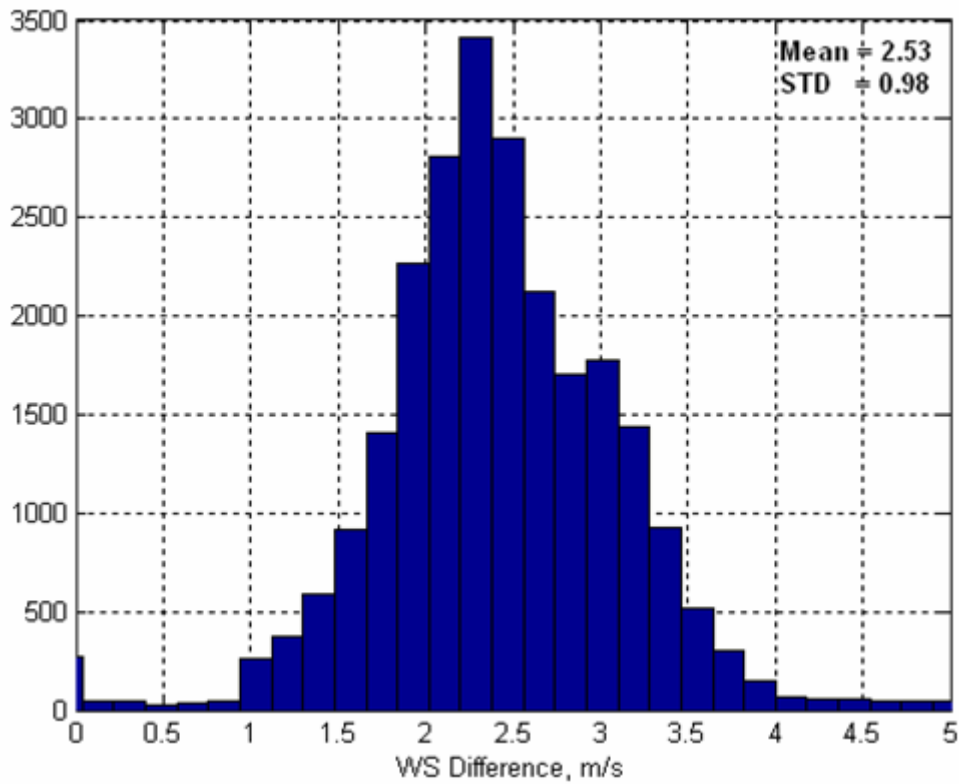
Figure 29 Histogram plot for the difference in HIRA retrieved WS values, m/s between SST =28 and 22°C.

4.3.2 Freezing Level

In hurricane radiative transfer modeling, the rain column is treated as extending up to the freezing level. TRMM studies (Fig. 30) have shown that the freezing level in the tropics varies between approximately 4.5 and 5.5 km. A sensitivity analysis was conducted using HIRA retrievals to determine the error sensitivity of *WS* and *RR* estimates to an assumed freezing level, or height of the rain column. Freezing level was varied between 4.25 and 6.05 km in these analyses.
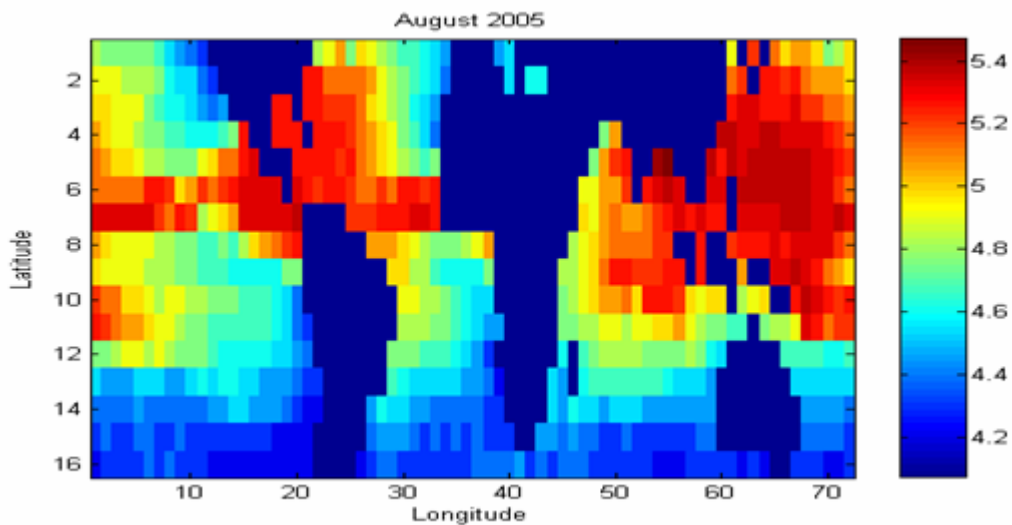
Figure 30 TRMM data between mid latitudes (±40°). The x and y axes are relative lat/long indices.

The reference or assumed "correct" value for freezing level that is used in this analysis is 4.65 km. This is the value that produces the best results in retrieval validation with the least difference in the HIRA *RR* retrieved values. Time series of the difference between the HIRA retrieved *WS* values for the variable freezing level compared to the

reference of 4.65 km were computed, as with *SST*. As an example, Fig. 31 shows the results of the of the rain rate difference time series for five eye wall penetrations for retrievals using a freezing level 6.05 km compared to the corresponding retrievals using 4.65 reference. The magnitude of the difference on the first pass was approximately 23 mm/hr. Similar comparisons were made for the wind speed retrievals. Again, the largest peak difference occurred where rain was located; so there is clearly a correlation between wind speed and rain rate errors. Over the range of considered freezing levels, the retrieved wind speed difference sensitivity to freezing level of 7 m/s per km and a retrieved rain rate difference sensitivity of approximately 13 mm/hr per km were observed. Maximum wind speed difference and maximum rain rate difference in the retrievals always occur at the maximum rain rate located in the eye wall region, as one would expect, since freezing level defines the depth of the rain column.
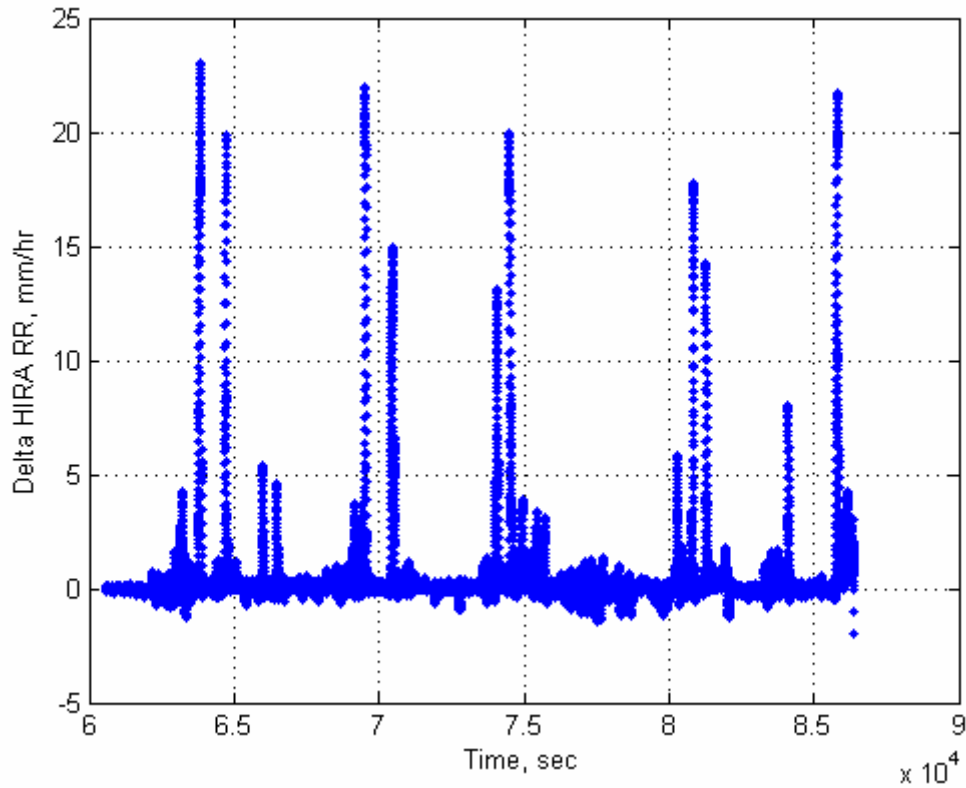
Figure 31 Delta HIRA retrieved RR values as a time series between freezing levels 4.65 and 6.05 km.

4.3.3   Water Vapor

Water vapor error sensitivity studies were done using the composite hurricane model of W. Frank [16]. Different temperature and relative humidity profiles were considered for four different cases where the radial distance from the center of the hurricane varied from the eye wall region out to approximately 700 km from the center of the storm. In W. Frank's model, hurricane atmospheres from a radial distance of 0.7 deg (delta/latitude) from the center of the eye out to 2, 4 and 6 degrees from the eye were used. According to the procedure described in Chapter 2, actual water vapor density profiles were computed and the surface water vapor values in gm/m^3 and scale heights in

km were obtained for use in generating inputs to HRad for each case. Temperature profile lapse rates were also computed for each case (APPENDIX A).

After comparing the HIRA retrieved wind speed and rain rate for each of these cases with retrievals using the atmosphere for the eye wall region (0.7 deg atmosphere) differences were calculated, and low sensitivities to water vapor were observed. For example, Fig. 32 is a plot of the difference in retrieved *WS* for r = 0.7 deg and r = 6 deg profiles. Comparing these values to the rest of the cases in the analysis for both wind speed and rain rate, there is a small sensitivity to water vapor similar to that found by [6] for SFMR retrievals. Errors of less than ± 2.5 m/sec and ± 1.5 mm/hr were observed for both the HIRA retrieved *WS* and *RR*, respectively, for the family of atmospheres considered. In general, the difference in HIRA retrieved *WS* increases as humidity decreases.
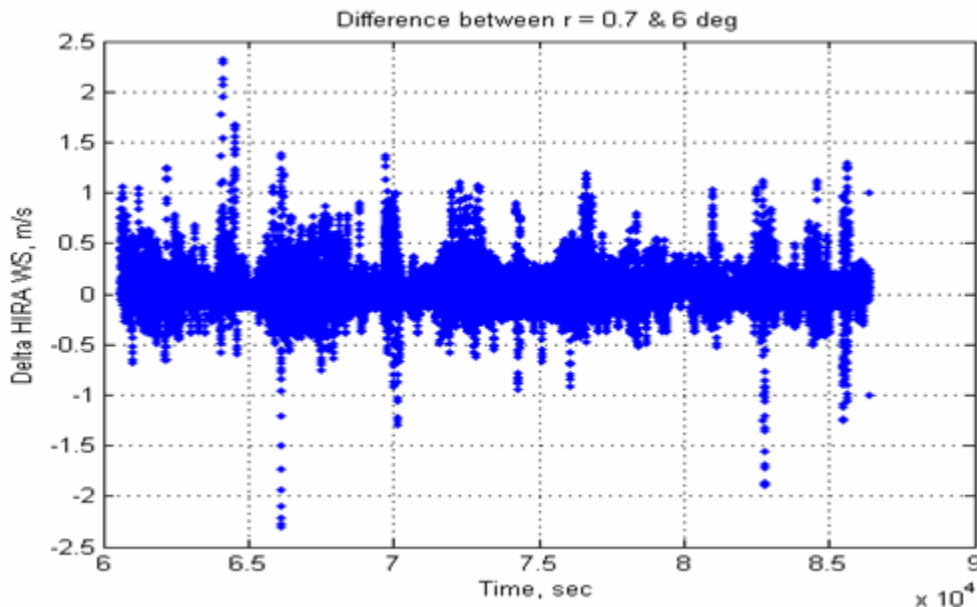
Figure 32 Delta HIRA retrieved WS values as a time series between radial distance 0.7 and 6 degrees.

In summary, these sensitivity studies demonstrate the importance of the role of *SST* and freezing level assumptions to the accuracy of *WS* and *RR* retrievals. They also show the relative insensitivity temperature and humidity profiles. These results are generally consistent with the findings in the SFMR wind speed and rain rate validation studies. Additional sensitivity studies are planned for cloud modeling and for the rain attenuation coefficient power law parameters.

CHAPTER 5 CONCLUSION

An algorithm for simultaneous retrieval of surface wind speed and rain rate in hurricanes from multi-frequency, C-band radiometric measurements (HIRA) has been developed, and the importance of rain effects in the modeling and retrieval of geophysical parameters in hurricanes has been demonstrated. HIRA is composed of a forward radiative transfer model, HRad, and a statistical least-squares difference inversion algorithm. Good results in comparing HIRA simultaneous wind speed and rain rate retrievals to those of the NOAA SFMR geophysical retrieval algorithm validate the performance of the HIRA model for the nadir viewing case.

Five hurricanes from 2003-2005 for a total of 22 flights were used to validate the HIRA algorithm. Representative results from hurricane Katrina, a category 5 storm in 2005, have been presented. Differences were computed between NOAA SFMR and HIRA algorithms and the resulting mean differences for wind speed and rain rate were 0.95 m/s and 0.53 mm/hr and the standard deviation of differences were 1.3 m/s and 1.58 mm/hr for wind speed and rain rate respectively. These observations lead to the conclusion that the HIRA model works well at nadir. Addition of an off nadir capability is planned for the future.

In hurricanes, the dominance of rain over other atmospheric contributors, such as water vapor and cloud liquid water, on radiometric brightness temperatures has been observed. Further, the sensitivity of T_b to surface emissions has been demonstrated. Sensitivity studies using the HIRA algorithm have demonstrated the importance of accurate knowledge of particular geophysical parameters, such as sea surface temperature

and altitude of the freezing level in the atmosphere, and the relative insensitivity to others, such as water vapor. Further sensitivity studies are planned.

A low sensitivity to sea surface temperatures errors of 0.6 m/s per deg C in the estimate of wind speed was observed for low rain regions and approximately 1.5 m/s per deg C in the high rain bands. In both regions, there was no rain rate error dependence, as expected. Since the atmospheric freezing level defines the top of the rain column in modeling rain, knowledge of the freezing level was considered. Significant retrievals sensitivities of *WS* and *RR* to freezing level of 7 m/s per km and 13 mm/hr were found in the high rain bands. Water vapor sensitivity was found to be relatively low. Water vapor profiles from the eye wall region out to approximately 700 km radial distance from the eye were compared and retrieval errors of less than $\pm$ 2.5 m/s and $\pm$ 1.5 mm/hr were observed for both the HIRA retrieved *WS* and *RR*, respectively. These results are consistent with similar sensitivity analyses conducted as part of SFMR validation.

Future plans call for integrating an improved surface wind speed model into HIRA that will perform well up to wind speeds of greater than 70 m/s, which also have incidence angle dependence. This model is required to support design and retrieval studies for the Hurricane Imaging Radiometer, HIRad. HIRad is an instrument concept that improves on the SFMR capability by providing a wide swath measurement compared to the SFMR nadir viewing profile of brightness temperature. HIRad is a synthetic aperture interferometric radiometer that will provide measurements over a swath equal to twice the aircraft altitude and will yield images of hurricane surface wind speed and rain rate in less than 4 passes from 10 km altitude. For high flying aircraft complete images can be produced with just 2 passes.

MONTE CARLO simulations and design studies are planned using the upgraded HIRA and numerical modeled wind speed and rain rate from hurricane Floyd, 1999. Geophysical noise will be simulated in the hurricane Floyd data and instrument noise will be added to the brightness temperature images. Sensitivity studies and error analyses will be done to define the performance of HIRad in various design trade studies.

APPENDIX A
THE HURRICANE ATMOSPHERE

Based on W. Frank composite hurricane atmosphere at 0.7 degrees from the eye, Table 2 shown earlier in Chapter 2 referred to the atmospheric model for hurricane eyewall region used in defining the hurricane atmosphere [16]. Table 3, refers to the used atmospheric water vapor profile.

Table 3 Atmospheric water vapor profile

Temp	Relative Humidity	Water Vapor Density	
(^{o}C)	(%)	Saturation (gm/m^3)	Actual (gm/m^3)
24.5	95	22.57	21.44
23.8	94	21.70	20.40
21.1	94	18.61	17.49
18.8	94	16.27	15.29
16.7	93	14.34	13.34
11.3	92	10.21	9.39
5.0	89	6.63	5.90
-2.3	91	3.89	3.54
-11.2	85	2.45	2.08
-24.0	77	-----	-----

The relative humidity defined by (2.21) is used to calculate for the actual vapor density where the saturated water vapor versus temperature is given in Table 4, and is previously shown in Fig. 15 of Chapter 2.

Table 4 Saturated vapor pressure density for water for r = 0.7 deg

Temp	Temp	Saturated Vapor Pressure	Saturated Vapor Density	Temp	Temp	Saturated Vapor Pressure	Saturated Vapor Density
(^{o}C)	(^{o}F)	(mmHg)	(gm/m^3)	(^{o}C)	(^{o}F)	(mmHg)	(gm/m^3)
-10	14	2.15	2.36	40	104	55.3	51.1
0	32	4.58	4.85	60	140	149.4	130.5
5	41	6.54	6.8	80	176	355.1	293.8
10	50	9.21	9.4	95	203	634	505
11	51.8	9.84	10.01	96	205	658	523
12	53.6	10.52	10.66	97	207	682	541
13	55.4	11.23	11.35	98	208	707	560
14	57.2	11.99	12.07	99	210	733	579
15	59	12.79	12.83	100	212	760	598
20	68	17.54	17.3	101	214	788	618
25	77	23.76	23	110	230	1074.6	-----
30	86	31.8	30.4	120	248	1489	-----
37	98.6	47.07	44	200	392	11659	7840

Figure 33 is a plot of the actual water vapor density, from the W. Frank based data, with a quadratic fit applied. According to Fig. 16, a surface density and a scale height were selected according to the applied exponential fit. A surface density of 23 gm/m^3 and a scale height of 3.5 km were the best fits according to (2.20).

The temperature profile in Tables 2 and 3 shows a freezing height of approximately 6 km which can be used to define the upper altitude for rain absorption and the height of the cloud tops.

The altitude data used in Tables 2 and 3 comes from [18].
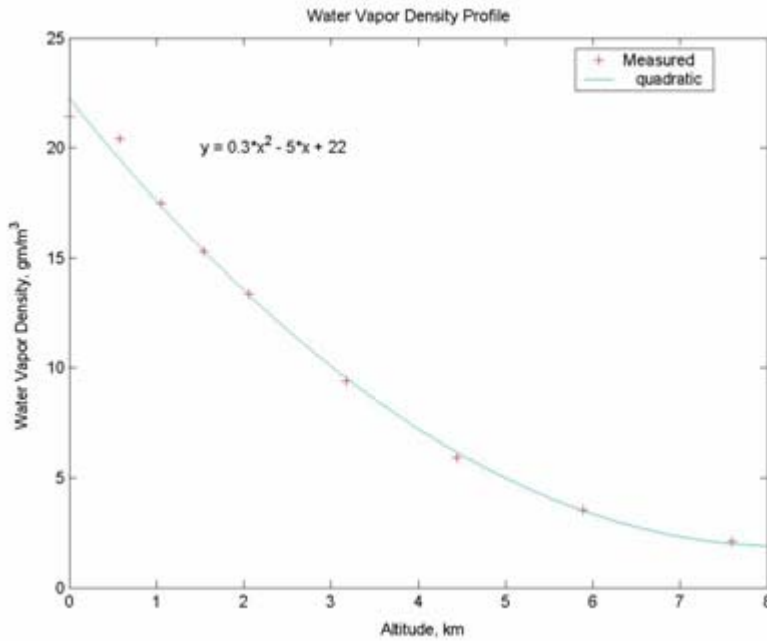
Figure 33 Actual water vapor density profile for W. Frank composite hurricane model at 0.7 degrees from the eye.

A lapse rate of – 4.8 was computed according to the atmospheric temperature profile for the W. Frank hurricane as shown previously in Fig. 17.

The same procedure was done for another three different cases for a radial distance 2, 4 and 6 deg. Table 5 shows the correspondent saturated and actual water vapor densities for a radial distance of 2 degrees.

Table 5 Saturated vapor pressure density for water for r = 2 deg

Pressure	Height		Temperature	Relative Humidity	Saturated Water Vapor Density	Actual Water Vapor Density
(mbar)	(meters)	(feet)	(^{o} C)	(%)	(gm/m^3)	(gm/m^3)
1000	0	0	25.7	90	24.128	21.715
950	583	1915	23.7	89	21.581	19.207
900	1054	3460	20.8	89	18.288	16.276
850	1547	5075	18.4	87	15.884	13.819
800	2063	6770	16.1	83	13.825	11.475
700	3182	10440	10.7	78	9.8119	7.6533
600	4442	14575	4.1	76	6.2155	4.7238
500	5888	19315	-3.2	70	3.6447	2.5513
400	7595	24920	-12.8	60	2.4287	1.4572
300	9682	31765	-27.0	53	6.4913	3.4404
250	10935	35875	-36.4	------	15.168	------
200	12396	40670	-48.7	------	38.255	------
150	14177	46510	-63.6	------	94.061	------
100	16568	54355	-75.5	------	171.38	------
80	------	------	-73.6	------	156.61	------
70	------	------	-67.7	------	116.81	------
60	------	------	-64.9	------	100.87	------
50	------	------	-60.9	------	81.031	------

The exponential approximation to the water vapor density profile resulted in a surface value of 22.79 gm/m^3 and scale height of 3.01 km. RadTb input in gm/cm^2 = 7.57 gm/cm^2. A Lapse Rate of -6.2 was found as well for this case.

Table 6 shows the correspondent saturated and actual water vapor densities for a radial distance of 4 degrees.

Table 6 Saturated vapor pressure density for water for r = 4 deg

Pressure	Height		Temperature	Relative Humidity	Saturated Water Vapor Density	Actual Water Vapor Density
(mbar)	(meters)	(feet)	(^{o} C)	(%)	(gm/m^3)	(gm/m^3)
1000	0	0	26.1	85	24.666	20.966
950	583	1915	23.7	84	21.581	18.128
900	1054	3460	20.9	83	18.394	15.267
850	1547	5075	18.4	79	15.884	12.548
800	2063	6770	16.0	74	13.741	10.168
700	3182	10440	10.6	66	9.7473	6.4332
600	4442	14575	3.7	64	6.0381	3.8644
500	5888	19315	-3.9	58	3.4711	2.0132
400	7595	24920	-14.0	50	2.4676	1.2338
300	9682	31765	-28.2	46	7.2743	3.3462
250	10935	35875	-38.0	------	17.311	------
200	12396	40670	-50.2	------	42.279	------
150	14177	46510	-64.6	------	99.269	------
100	16568	54355	-76.4	------	178.74	------
80	------	------	-73.4	------	155.11	------
70	------	------	-68.7	------	122.95	------
60	------	------	-65.2	------	102.5	------
50	------	------	-61.1	------	81.946	------

The exponential approximation to the water vapor density profile resulted in a surface value of 21.70 gm/m^3 and scale height of 2.90 km. RadTb input in gm/cm^2 = 7.48 gm/cm^2. A Lapse Rate of -5.3 was found as well for this case.

Table 7 shows the correspondent saturated and actual water vapor densities for a radial distance of 6 degrees.

Table 7 Saturated vapor pressure density for water for r = 6 deg

Pressure	Height		Temperature	Relative Humidity	Saturated Water Vapor Density	Actual Water Vapor Density
(mbar)	(meters)	(feet)	(^{o} C)	(%)	(gm/m^3)	(gm/m^3)
1000	0	0	25.7	83	24.128	20.026
950	583	1915	23.1	80	20.863	16.69
900	1054	3460	20.2	80	17.661	14.129
850	1547	5075	17.8	75	15.325	11.494
800	2063	6770	15.5	68	13.325	9.0608
700	3182	10440	10.2	57	9.4925	5.4107
600	4442	14575	3.3	54	5.865	3.1671
500	5888	19315	-4.7	50	3.2883	1.6442
400	7595	24920	-14.9	43	2.528	1.087
300	9682	31765	-29.3	39	8.0672	3.1462
250	10935	35875	-39.1	------	18.916	------
200	12396	40670	-51.0	------	44.552	------
150	14177	46510	-65.0	------	101.41	------
100	16568	54355	-76.4	------	178.74	------
80	------	------	-74.1	------	160.4	------
70	------	------	-68.6	------	122.32	------
60	------	------	-65.4	------	103.59	------
50	------	------	-61.8	------	85.212	------

The exponential approximation to the water vapor density profile resulted in a surface value of 19.89 gm/m^3 and scale height of 2.50 km. RadTb input in gm/cm^2 = 7.96 gm/cm^2. A Lapse Rate of -5.3 was found as well for this case.

APPENDIX B
SFMR DESCRIPTION

The NOAA/Hurricane Research Division's (HRD) Stepped Frequency Microwave Radiometer (SFMR) is the prototype for a new generation of airborne remote sensing instruments designed for operational surface wind estimation in hurricanes. It was first flown in hurricane Allen in 1980 as reported in Jones et al. (1981) [5], Black and Swift (1984) [19] and Delnore et al. (1985) [20]. In the mid-1980's the instrument was redesigned and flown on the NOAA Hurricane Research WP-3 aircraft, and the first real-time retrieval of winds on board the aircraft in Hurricane Earl in 1985 as reported by Swift and Goodberlet (1992) [21]. The first operational transmission of SFMR winds to TPC/NHC occurred in Hurricane Dennis in 1999. Since 1980, the SFMR has flown on 95 flights in 30 tropical cyclones.

The concept for the first experimental SFMR was proposed by C. T. Swift and built by NASA's Langley Research Center in 1978. The original SFMR design involved a single nadir-viewing antenna and receiver capable of making measurements of radio emission from the sea surface at four selectable frequencies 4.5, 5.0, 5.6, and 6.6 GHz. After 1981, the program was transferred to the University of Massachusetts Microwave Remote Sensing Laboratory (UMASS/MIRSL); and SFMR was updated in 1982 to six different frequencies with a better delta-T resolution and longer integration time.

The SFMR receiver was upgraded in 1995 which allowed for increased calibration stability, and used six different channels (4.55, 5.06, 5.64, 6.34, 6.96 and 7.22 GHz) with an along-track nadir-viewing antenna. Since the antenna half-power beamwidth ranges from 22° to 32°, at a typical flight altitude of 1500 m, the six C-band

channels view the surface with antenna footprints from 600 to around 800 m depending upon the channel.

The SFMR instruments are mounted on two different places on the aircraft body, the first place is the bottom of the aircraft and that is the SFMR research instrument, as for the AOC SFMR, it is mounted in a pod under the aircraft wing as shown in Fig. 34.
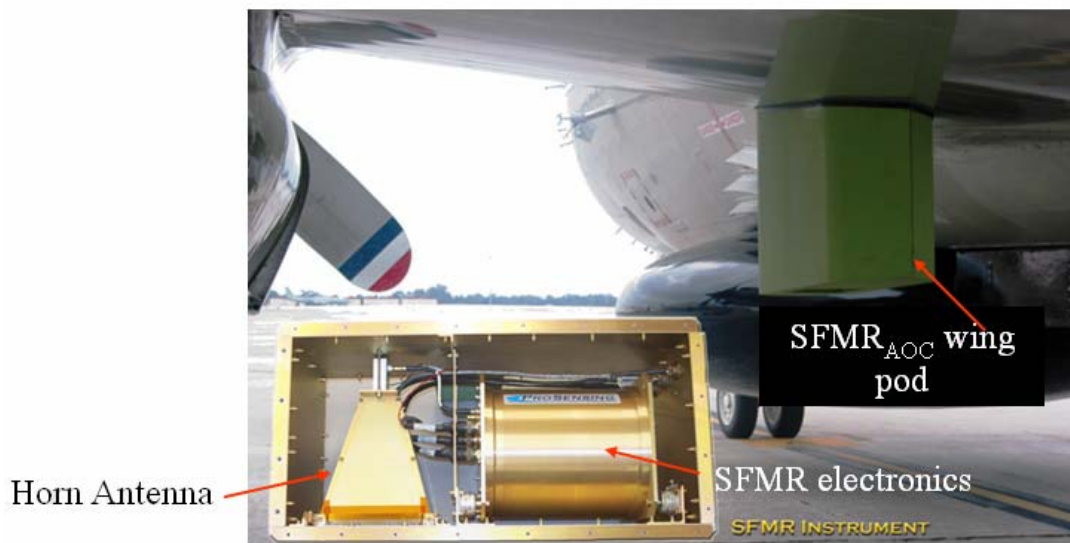
Figure 34 AOC SFMR instrument electronics.

.

Table 8 and Table 9 contain the SFMR research instrument beamwidth and the AOC SFMR instrument beamwidth, respectively. The main difference between the two is the way they are mounted under the aircraft which is very important since one is parallel with the plane of incidence at nadir and the other is perpendicular to the plan of incidence at nadir. Another difference is the beam width of the antenna; the AOC instrument has less integration time and more calibrated channels.

Table 8 Antenna gain pattern for the SFMR research instrument

Frequency (GHz)	H-Plane	E-Plane	45 – Plane
4.3	16.2	16.7	16.1
4.8	16	16.2	15.3
5.3	15.7	15.5	14.8
5.8	5.5	16	14.6
6.3	16.8	20	16.9
6.8	19	16.5	17.6

Table 9 Antenna gain pattern for the AOC SFMR instrument

Frequency (GHz)	3 dB Beamwidth
5	28
6	23
7	19

APPENDIX C
RADTB MICROWAVE RADIATIVE TRANSFER MODEL

This appendix describes the microwave RTM named RadTb, which is used at the Central Florida Remote Sensing Laboratory. This model was derived from the EnvaMod RTM [22] that was developed by the US Naval Research Laboratory during the 1970's. RadTb calculates brightness temperature for a defined operating frequency and incidence angle as a function of 14 physical properties of the ocean and intervening atmosphere. RadTb is a FORTRAN program that consists of a main program and subroutines that will be discussed in details. Subroutine names are inconsistent with Fig. 22 physical model where the exact names used in the original FORTRAN program are used in this appendix.

The main program sets initial conditions and outputs results as a .TXT file. It calls INPUT subroutine, ATMOS subroutine and then calls SEAMOD subroutine. The calculated brightness temperatures are then displayed in the .TXT output file.

INPUT subroutine inputs the radiometer and environmental parameters. This subroutine reads a text input file textinput.txt. The input environmental file is a matrix of size (m x 14) where each row constitutes a new RTM calculation or pixel in the collocation box. The input parameters are:

Radiometer parameters:

FREQ – frequency (GHz)

THETA – incidence angle (º)

HOBS – height of observer (km)

Environmental parameters:

PS – surface pressure (mb)

TSC – surface air temperature (° C)

RLAPSE – air temperature vertical lapse rate (° C/km)

AHS – surface absolute humidity (g/m3)

H2OV – columnar density of water vapor (g/cm^2)

TTP – temperature of the tropopause (K)

MIXRAT – water vapor mixing ratio above the tropopause

H2OL – columnar density of cloud water (g/cm^2)

HCB – height of cloud base (km)

HCT – height of cloud top (km)

RAINR – rain rate (mm/hour)

WMPS – surface wind speed (m/s)

TSEAC – sea surface water temperature (° C)

SALIN – sea surface salinity (ppt).

ATMOS subroutine calculates the loss (transmission coefficient) and self–emission (upwelling and downwelling brightness temperature) of the atmosphere along a slant path propagation that is defined by an observer looking down at a surface incidence angle, THETA, from a height HOBS in the atmosphere.

The input parameters are:

FREQ – frequency (GHz)

THETA – incidence angle (º)

HOBS – height of observer (km)

PS – surface pressure (mb)

TSC – surface air temperature (º C)

RLAPSE – air temperature vertical lapse rate (º C/km)

AHS – surface absolute humidity (g/m^3)

H2OV – columnar density of water vapor (g/cm^2)

TTP – temperature of the tropopause (K)

MIXRAT – water vapor mixing ratio above the tropopause

H2OL – columnar density of cloud water (g/cm^2)

HCB – height of cloud base (km)

HCT – height of cloud top (km)

Output parameters are:

HWV – water vapor scale height (km)

RHS – relative humidity at the surface (%)

MCMAX – max cloud water density (g/m^3)

HTP – height of the tropopause (km)

CH2OV – calculated columnar water vapor density (g/cm^2)

CH2OL – calculated columnar cloud water density (g/cm^2)

TUPS – sky radiation seen looking up from surface (K)

TUP – sky radiation seen looking up from HOBS (K)

TDOWN – sky radiation seen looking down from HOBS (K)

LOSTL – total atmospheric loss (transmission coefficient)

LOSDN – atmospheric loss from HOBS to surface

ATMOS calls subroutines: PRODEF, ABSH2O, ABSO2, ACLOUD, DIECON, TDNATM, and TUPATM.

PRODEF subroutine defines atmospheric levels and environmental variable profiles. The input parameters that go to PRODEF are:

THETA – incidence angle (º)

HOBS – height of the observer (km)

PS – surface pressure (mb)

TSC – surface air temperature (º C)

RLAPSE – air temperature vertical lapse rate (º C/km)

AHS – surface absolute humidity (g/m^3)

H2OV – columnar density of water vapor (g/cm^2)

TTP – temperature of tropopause (K)

MIXRAT – water vapor mixing ratio above tropopause

H2OL – columnar density of cloud water (g/cm^2)

HCB – height of cloud base (km)

HCT – height of cloud top (km)

NL – number of levels

DH – increments between levels (km)

The output parameters are:

H – height of levels (km)

DHC – corrected increments between levels (km)

P – pressure profile (mb)

T – temperature profile (K)

RHO – air density profile (g/m^3)

AH – absolute humidity profile (g/m^3)

MC – density of cloud liquid water profile (g/m^3)

LHOB – level equal to or just above hobs

HWV – water vapor scale height (km)

RHS – relative humidity at the surface (%)

MCMAX – max cloud water density (g/m^3)

HTP – height of tropopause

CH2OV – calculated columnar water vapor density (g/cm^2)

CH2OL – calculated columnar cloud water density (g/cm^2)

The absorption coefficients due to water vapor, cloud liquid water and oxygen are then calculated using three different subroutines; ABSH2O, ACLOUD and ABSO2. The

rain rate absorption coefficient is being calculated in a MATLAB program and all four absorption coefficients are being summed up in the same MATLAB program as well.

ABSH2O subroutine calculates the absorption coefficient of water vapor in air by means of Gross's formula [11] from frequencies below 400 GHz. It approximates contribution from higher frequency vapor lines by low frequency from line shape function. Empirical correction for wings of infrared absorption added. The input parameters to ABSH2O are:

L – level number

P – total pressure at L (mb)

T – temperature at L (K)

AH – absolute humidity at L (g/m^3)

FREQ – frequency (GHz)

The output parameter is the absorption coefficient at L (Np/km), ALH2O.

ACLOUD subroutine calculates cloud absorption coefficient at level L. Rayleigh scattering is assumed. The input parameters are:

L – level number

T – temperature at L (K)

MC – liquid water density at L (g/m^3)

FREQ – frequency (GHz)

The output parameter is the absorption coefficient at L (Np/km), ALCLD.

ABSO2 subroutine calculates molecular oxygen absorption at level L. The results of ROSENKRANZ (1975) are used. The input parameters are:

L – level number

P – total pressure at L (mb)

T – temperature at L (K)

FREQ – frequency (GHz)

The output parameter is the oxygen absorption coefficient at L (Np/km), ALO2 (L).

These absorption coefficients are summed and used as input to ATMOS subroutine. Both the TDNATM and the TUPATM are also subroutines that interact with the main ATMOS subroutine.

TDNATM subroutine calculates the down–welling atmospheric emission looking down from any level. The input parameters are:

LEVEL – level number

T – temperature profile (K)

ALTOT – atmospheric absorption profile (Np/km)

LTOT – loss profile

DHC – layer thickness (km)

The output parameter is the atmospheric emission looking down from level (K), TDNEM.

TUPATM subroutine calculates the atmospheric emission looking up from any level. The input parameters are:

LEVEL – level number

T – temperature profile (K)

ALTOT – atmospheric absorption profile (Np/km)

LTOT – loss profile

DHC – layer thickness (km)

The output parameter is the atmospheric emission looking up from level (K), TUPEM.

The output of the ATMOS subroutine then goes into the main program that calls the SEAMOD subroutine which is called by the DIECON subroutine.

DIECON subroutine calculates the complex dielectric properties of seawater. NRL fitted parameters are used. The input parameters are:

S – salinity (ppt)

T – temperature at L (K)

FREQ – frequency (GHz)

The output parameters are the real and imaginary parts of dielectric constant, E1and E2.

SEAMOD subroutine uses the complex dielectric constant of seawater to calculate the specular Fresnel power reflection coefficient (and emissivity) of the air–sea

interface. Empirical equations are used to define multiplicative roughness reflection coefficients of a wind driven sea. The input parameters are:

FREQ – frequency (GHz)

THETA – incidence angle (º)

WMPS – surface wind speed (m/s)

TSEAC – sea temperature (º C)

SALIN – sea salinity (ppt)

The output parameters are:

RSPEC – reflection coefficient for a specular sea

RRUFF – reflection coefficient for a rough sea without foam

RFOAM – reflection coefficient for foam covered sea

FOMFR – fraction of sea covered with sea foam

MATLAB CODES

```matlab
% Program # 1
% HRad Forward Model
% Calculating the atmospheric absorption coefficients & all the atmospheric components

% Definitions
% theta: Incidence Angle
% freq: SFMR Six Frequencies [4.74 5.31 5.57 6.02 6.69 7.09]
% HOBS: Height of the Observer
% SST: Sea Surface Temperature (Retrieved)
% WS: Wind Speed (Retrieved)
% RR: Rain Rate (Retrieved)
% WV: Water Vapor (gm/m^3)
% s: Salinity (ppt)

% Loading the absorption coefficients
load testcaseoutSFMR_BOX_H2OL_00;
k_474=testcaseoutSFMR_BOX_H2OL_00(1,5:43);
k_531=testcaseoutSFMR_BOX_H2OL_00(2,5:43);
k_557=testcaseoutSFMR_BOX_H2OL_00(3,5:43);
k_602=testcaseoutSFMR_BOX_H2OL_00(4,5:43);
k_669=testcaseoutSFMR_BOX_H2OL_00(5,5:43);
k_709=testcaseoutSFMR_BOX_H2OL_00(6,5:43);

% WS Range 1-100 m/s, RR Range 1-100 mm/hr
counter=0;
for freq=[4.74 5.31 5.57 6.02 6.69 7.09]
    counter=counter+1
```

```
FREQ=[474 531 557 602 669 709];
HOBS=3.7;
SST=28;
WV=23;
eval(['result',int2str(FREQ(counter)),'=zeros(91,100);'])
load input;
```

% Including the altitude (HOBS)
```
tkn=0;
for bl=1:39
    tkn=tkn+tk(bl);
    if tkn>=HOBS
        blr=bl;
        break
    end
    blr=bl;
end
sum(tk);
Tatmos=T;
clear T K_10 K_18 K_23 K_37;
number=1;
for RR=0:1:100;
    RR
    WS=0:1:100;
```

% Adding RR absorption coefficient to the total absorption coefficient
```
kr=1.87e-6*RR.^(1.15).*freq.^(2.6*RR.^0.0736);
eval(['add=kr+k_',int2str(FREQ(counter)),'(1,1:29);'])
eval(['k',int2str(FREQ(counter)),'=k_',int2str(FREQ(counter)),';'])
eval(['k',int2str(FREQ(counter)),'(1,1:29)=add;'])
eval(['k_RTM_',int2str(FREQ(counter)),'=k',int2str(FREQ(counter)),';'])
eval(['x=k_RTM_',int2str(FREQ(counter)),';'])
```

%Setting Parameters
    theta=(0)*pi/180;

%Finding the range R in km which equals to the thickness 'tk'
% Multiply by the sec of theta for the slant range
    eval(['R',int2str(FREQ(counter)), '_',int2str(WV),'=tk.*sec(theta*pi/180);'])

% Finding Transmissivity L
     eval(['L',int2str(FREQ(counter)),'_',int2str(WV),'=x.*R',int2str(FREQ(counter)),'_',int2str(WV),';'])

% Converting the transmissivity to power ratio 't'
    eval(['t',int2str(FREQ(counter)),'_',int2str(WV),'=exp(-L',int2str(FREQ(counter)),'_',int2str(WV),');'])

% Emissivity per layer 'e'
    eval(['e',int2str(FREQ(counter)),'_',int2str(WV),'=1-t',int2str(FREQ(counter)),'_',int2str(WV),';'])

% Brightness temperature per layer 'T_new' (Kelvin)
    eval(['T_new=Tatmos.*e',int2str(FREQ(counter)),'_',int2str(WV),';'])

% Calculating T_{DOWN} and T_{SKY}
    c1=38;
    c2=0;
    Tsky=0;
    c3=1;
    s1=zeros(38,1);
    for m=39:-1:2
       Tsky=Tsky+c2;
       c4=T_new(m);
       if c1>1
          for n=c1:-1:1

```matlab
        eval(['c2=c4.*t',int2str(FREQ(counter)),'_',int2str(WV),'(n);'])
            c4=c2;
        end
    else
        eval(['c2=c4*t',int2str(FREQ(counter)),'_',int2str(WV),'(c1);'])
    end
    s1(c3)=c2;
    c3=c3+1;
    c1=c1-1;
end
Tsky=Tsky+c2;
Tdown=Tsky+T_new(1);
c5=1;
for s=39:-2:3
eval(['c=t',int2str(FREQ(counter)),'_',int2str(WV),'(s)*t',int2str(FREQ(counter)),'_',int2str(WV),'(s-1);'])
    c5=c*c5;
end
eval(['c5=c5*t',int2str(FREQ(counter)),'_',int2str(WV),'(1);'])
tau=c5;
Tsky=Tdown+2.7*tau;

% Calculating Tup
c6=2;
c7=0;
Tup=0;
for m=1:blr
    Tup=Tup+c7;
    c8=T_new(m);
        for n=c6:blr
            eval(['c7=c8*t',int2str(FREQ(counter)),'_',int2str(WV),'(n);'])
            c8=c7;
        end
```

96

```matlab
            c6=c6+1;
        end
        Tup=Tup+c7;
        Tup=Tup+T_new(blr);
% Total Tau
        c9=0;
        for jj=1:39
            eval(['rrr=c9+L',int2str(FREQ(counter)),'_',int2str(WV),'(jj);'])
            c9=rrr;
        end
        eval(['t',int2str(FREQ(counter)),'_',int2str(WV),'=exp(-c9);'])
        f=freq*1e9;
        T=SST;
        s=32;
        ff=f/1e9;


% Calculating the real and imaginary parts of the dielectric constant
        diimag=Sea_I(ff,T,s);
        direal=Sea_R(ff,T,s);


% Dielectric constant
        er2=direal-i*diimag;


% Power reflection coefficient
        IE=(0)*pi/180;
        rov=-1*((er2.*cos(IE))-(sqrt(er2-(sin(IE)).^2)))./((er2.*cos(IE))+(sqrt(er2-
(sin(IE)).^2)));
        roh=((cos(IE))-(sqrt(er2-(sin(IE)).^2)))./((cos(IE))+(sqrt(er2-(sin(IE)).^2)));
        gammav=(abs(rov)).^2;
        gammah=(abs(roh)).^2;
        clear s er2 IE rov roh
        WS=WS;
        RSM=gammah;
```

```matlab
% NOAA SFMR WS Model
    ff=f/1e9;


% WS < 33.2
    eew(1:34)=(1-RSM)+(5305.7987e-5+333.132252e-5*(WS(1:34)-
33.2)+5.2210144e-5*(WS(1:34)-33.2).^2)*(1+0.15*ff);


% WS > 33.2
    eew(35:101)=(1-RSM)+(5305.7987e-5+333.132252e-5*(WS(35:101)-
33.2))*(1+0.15*ff);
    TbHe=eew.*T;
    Tbsce=(1-eew).*Tsky;
    TatHe=tau.*(Tbsce+TbHe);
    Tap_e=Tup+TatHe;


% Polyfit to increase the resolution
    [P U]=polyfit(WS,Tap_e,3);
    eval(['Extreme_',num2str(FREQ(counter)),'(number,:)=P;'])
    number=number+1;
  end
end
save    matrix_combines    Extreme_474    Extreme_531    Extreme_557    Extreme_602
Extreme_669 Extreme_709


% Program #2
% HIRA Retrieval Algorithm


% Load the modeled Tb matrix
load matrix_combines


% Load SFMR measurement brightness temperatures
load Tb_1_Time_Tb_10_new_2
```

```
for Data_Set=1:28279
    Data_Set
    Tb=tB(Data_Set,:);
    Tb=Tb';
    Tb1=Tb(1);
    Tb2=Tb(2);
    Tb3=Tb(3);
    Tb4=Tb(4);
    Tb5=Tb(5);
    Tb6=Tb(6);
    dif_474=Tb1-result474;
    dif_531=Tb2-result531;
    dif_557=Tb3-result557;
    dif_602=Tb4-result602;
    dif_669=Tb5-result669;
    dif_709=Tb6-result709;
    squar1=dif_474.^2;
    squar2=dif_531.^2;
    squar3=dif_557.^2;
    squar4=dif_602.^2;
    squar5=dif_669.^2;
    squar6=dif_709.^2;
    all_sum_dif=squar1+squar2+squar3+squar4+squar5+squar6;
    min_dif=min(min(all_sum_dif));
    if min_dif==0
        [RR,WS]=find(all_sum_dif==0);
    else
        [RR,WS]=find(all_sum_dif==min_dif);
    end
    RR_WS_Retrieved(1,Data_Set)=RR+1;
    RR_WS_Retrieved(2,Data_Set)=WS+1;
end
save RR_WS_Retrieved RR_WS_Retrieved
```

LIST OF REFERENCES

[1] Y. Sun, "Evaluation of a Microwave Radiative Transfer Model using Satellite Radiometer Observations," in *School of Electrical Engineering and Computer Science*, vol. MS. Orlando: University of Central Florida, 2003.

[2] S. D. Thompson, "Evaluation of a Microwave Radiative Transfer Model for Calculating Satellite Brightness Temperature," in *School of Electrical Engineering and Computer Science*, vol. MS. Orlando: University of Central Florida, 2004.

[3] F. T. Ulaby, R. K. M. Moore, and A. K. Fung, *Microwave Remote Sensing, Active and Passive*, vol. 1. Norwood, MA: Artech House Inc, 1981.

[4] NASA, "Mariner to Mercury, Venus and Mars," California Institute of Technology, Pasadena, CA 1963.

[5] W. L. Jones, P. G. Black, V. E. Delnore, and C. T. Swift, "Airborne microwave remote-sensing measurements of Hurricane Allen," *Science*, vol. 214, pp. 274-280, 1981.

[6] E. W. Uhlhorn and P. G. Black, "Verification of Remotely Sensed Sea Surface Winds in Hurricanes," *J. Atmos. Oceanic Technol.*, pp. 100-115, 2003.

[7] J. W. Johnson, R. A. Amarin, S. F. El_Nimri, W. L. Jones, and M. C. Baileym, "A Wide-Swath Hurricane Imaging Radiometer For Airborne Operational Measurements," in *IGARSS*. Denver, Colorado, 2006.

[8]   L. A. Klein and C. T. Swift, "An improved model for the dielectric constant of sea water at microwave frequencies," *IEEE J. Oceanic Eng.*, vol. 2, pp. 104-111, 1977.

[9]   P. Debye, "Polar Molecules," *Chemical Catalog.*, 1929.

[10]   J. H. Van Vleck and V. F. Weisskopf, "On the Shape of Collision-Broadened Lines," *Rev. Mod. Phys.*, vol. 17, pp. 227-236, 1945.

[11]   E. P. Gross, "Shape of Collision-Broadened Spectral Lines," *Phys. Rev.*, vol. 97, pp. 395-403, 1955.

[12]   M. L. Meeks and A. E. Lilley, "The Microwave Spectrum of Oxygen in the Earth's Atmosphere," *Geophys. Res.*, vol. 68, pp. 1683-1703, 1963.

[13]   D. P. Jorgensen and P. T. Willis, "A Z-R Relationship for Hurricanes," Journal of Applied Meteorology," vol. 21, pp. 356-366, 1982.

[14]   R. L. Olsen, D. V. Rogers, and D. B. Hodge, "The aRb Relation in the Calculation of Rain Attenuation," *IEEE Trans. Antennas Propagat.*, vol. 26, pp. 318-329, 1978.

[15]   T. Wilheit, "Humidity over Ocean." Orlando, 2006.

[16]   W. M. Frank, "The Structure and Energetics of the Tropical Cyclone I. Storm Structure," *Mon. Wea. Rev.*, vol. 105, pp. 1119-1135, 1977.

[17]   H. Jiang, P. G. Black, E. J. Zipser, F. D. Marks JR., and E. W. Uhlhorn, "Validation of Rain-Rate Estimation in Hurricanes from the Stepped Frequency Microwave Radiometer: Algorithm Correction and Error Analysis," *Atmospheric Sciences*, vol. 63, pp. 252-267, 2006.

[18]   C. L. Jordan, "Mean Soundings for the West Indies Area," *J. Meteor.*, vol. 15, pp. 91-97, 1958.

[19]   P. G. Black and C. T. Swift, "Airborne stepped frequency microwave radiometer measurements of rainfall rate and surface wind speed in hurricanes," presented at Second Conf. on Radar Meteorology, Zurich, Switzerland, 1984.

[20]   V. E. Delnore, G. S. Bahn, W. L. Grantham, R. F. Harrington, and W. L. Jones, "Active and passive measurements in Hurricane Allen," NASA Tech. Rep. 1985.

[21]   M. A. Goodberlet and C. T. Swift, "Passive microwave remote sensing of the ocean," DOC/NOAA/ERL/WPL, Boulder, CO 1992.

[22]   M. M. a. Wisler and J. P. Hollinger, "Estimation of Marine Environmental Parameters using Microwave Radiometric Remote Sensing Systems," DOC/NOAA/ERL/WPL, Wash. D.C Nov. 1977.